

PRISM: Breaking the $O(n)$ Memory Wall in Long-Context LLM Inference via $O(1)$ Photonic Block Selection

Hyoseok Park¹ and Yeonsang Park^{1,*}

¹*Department of Physics, Chungnam National University, Daejeon 34134, Republic of Korea*

(Dated: March 24, 2026)

Long-context LLM inference is bottlenecked not by compute but by the $O(n)$ memory bandwidth cost of scanning the KV cache at every decode step—a wall that no amount of arithmetic scaling can break. The semiconductor industry increasingly acknowledges this shift: NVIDIA’s Vera Rubin architecture dedicates an entire DPU (ICMS) to KV cache management with flash-backed storage and hardware-assisted prefetch—an architectural bet confirming that memory, not arithmetic, is the first-class constraint.

Recent photonic accelerators have demonstrated impressive throughput for dense attention computation. However, these approaches inherit the same $O(n)$ memory scaling as electronic attention when applied to long contexts. We observe that the real leverage point is the coarse block-selection step: a memory-bound similarity search that determines which KV blocks to fetch. We identify, for the first time, that this task is *structurally matched* to the photonic broadcast-and-weight paradigm—the query fans out to all candidates via passive splitting, signatures are quasi-static (matching electro-optic MRR programming), and only rank order matters (relaxing precision to 4–6 bits). Crucially, the photonic advantage *grows with context length*: as N increases, the electronic scan cost rises linearly while the photonic evaluation remains $O(1)$.

We instantiate this insight in PRISM (**P**hotonic **R**anking via **I**nnner-product **S**imilarity with **M**icroring weights), a thin-film lithium niobate (TFLN) similarity engine. Hardware-impaired needle-in-a-haystack evaluation on Qwen2.5-7B confirms 100% accuracy from 4K through 64K tokens at $k=32$, with $16\times$ traffic reduction at 64K context. PRISM achieves a four-order-of-magnitude energy advantage over GPU baselines at practical context lengths ($n \geq 4K$).

INTRODUCTION

The dominant cost of large language model (LLM) inference is no longer floating-point arithmetic. As autoregressive decoding generates one token at a time, each step requires reading the full key–value (KV) cache accumulated over all previous tokens, computing attention scores, and writing the result back. For a model with L layers and H attention heads, each storing key and value vectors of dimension d_h , the KV cache occupies $2LHd_h$ bytes per token (at half precision), growing linearly with context length n . At $n = 128\,000$ tokens, a 70-billion-parameter model’s KV cache can exceed 40 GB—comparable to the entire model weight footprint—and the memory bandwidth required to stream this cache at every decode step far exceeds the compute throughput of modern GPUs [1].

This memory wall is intensifying [2]. Context windows are expanding at an unprecedented pace: GPT-5.4 [3] and Claude Opus 4.6 [4] now support one million tokens, Gemini 2.5 Pro extends to one million with native multimodal processing [5], Meta’s Llama 4 Scout pushes the frontier to 10 million tokens with a mixture-of-experts architecture [6], and Qwen2.5 similarly extends to one million [7]. Multi-agent and retrieval-augmented generation (RAG) workloads routinely concatenate documents

into contexts of hundreds of thousands to millions of tokens. NVIDIA’s response in its Vera Rubin architecture is telling: the *Intelligent Connectivity and Memory Switch* (ICMS), built on the BlueField-4 data processing unit (DPU), adds a flash-based KV cache tier that can hold terabytes of context, together with hardware-assisted eviction and prefetch logic [8, 9]. This architectural bet confirms that KV cache management is now a first-class system design problem.

Recent photonic accelerators have demonstrated impressive throughput for dense attention computation [10–13]. In particular, Tian et al. demonstrated a photonic transformer chip (PTC) achieving over 200 POPS for full attention via coherent Mach–Zehnder meshes [12]. However, these approaches target dense matrix–vector multiplication and inherit the same $O(n)$ memory scaling as electronic attention when applied to long contexts—every KV entry must still be transferred to the photonic chip. Electronic block-selection methods (Quest [14], RocketKV [15]) reduce the number of blocks *fetched*, but the selection scan itself—computing similarity scores across all N candidates—still traverses the memory hierarchy at $O(N)$ cost. Neither photonic dense computation nor electronic sparse selection breaks the linear scaling. The fundamental bottleneck is therefore not attention computation, but the *selection scan itself*: the $O(N)$ memory read required to evaluate all candidate blocks. Eliminating this scan—rather than merely reducing the number of blocks fetched—changes the scaling from $O(N)$ to $O(k)$, independent of the total number of cached

¹ Corresponding author: yeonsang.park@cnu.ac.kr

blocks. We observe that the coarse block-selection step is a memory-bound similarity search that determines which of $N \sim 10^3\text{--}10^4$ KV blocks to fetch. This search has three properties that are *structurally matched* to the photonic broadcast-and-weight (B&W) paradigm [16, 17]: (i) the query fans out identically to all candidates, mapping directly to passive optical splitting; (ii) stored block signatures are quasi-static (updated every 64–512 tokens), matching fast MRR electro-optic programming (Pockels effect); and (iii) only rank order matters, relaxing precision to 4–6 bits. Crucially, the photonic advantage *grows with context length*: as N increases, the electronic scan cost rises linearly while the photonic evaluation latency remains $O(1)$ (though the hardware footprint scales as $O(d \times N)$ MRRs).

In the B&W architecture, a WDM laser comb encodes a d -dimensional query onto d co-propagating wavelengths; a $1 \times N$ passive splitter broadcasts identical copies to N channels; a bank of microring resonators (MRRs) on thin-film lithium niobate (TFLN) applies programmable weights at each channel; and a broadband photodetector integrates over all wavelengths, yielding the analog inner product in $O(1)$ optical latency. We therefore propose *scan-free block selection*—eliminating the $O(N)$ memory read entirely—and instantiate this principle using a photonic broadcast-and-weight engine, where the natural broadcast property of optics makes scan-free selection physically native to the hardware. The resulting system is not a general neural-network accelerator, but a specialized similarity engine for the memory-bound block-selection task.

A crucial observation simplifies the problem. Not all attention heads actually need the full cache. Recent work on *retrieval heads* [18–20] has shown that attention heads split into two categories: *retrieval* heads that attend to tokens far from the current position, and *streaming* heads that attend primarily to nearby tokens and “attention sinks.” The fraction classified as retrieval heads is threshold-dependent: DuoAttention identifies approximately 25% of heads as retrieval heads in MHA models and approximately 50% in GQA models via learned gating optimization [19], while our profiling on Qwen2.5-7B finds over 90% at a relaxed threshold ($\tau=0.3$; Sec.). This discrepancy reflects differing identification criteria rather than a contradiction—the key insight is that only the retrieval subset requires distant block fetches.

This asymmetry has motivated a family of *block-level selection* methods that implement a coarse candidate selection step followed by fine attention over only the selected blocks on the GPU [14, 15, 21–23]. Complementary strategies include token-level eviction (H₂O [24], StreamingLLM [25, 26]), two-stage coarse-fine retrieval (RocketKV [15]), and hardware-assisted caching (NVIDIA ICMS [9]). All electronic approaches share a common limitation: the coarse selection step itself consumes memory bandwidth proportional to the number of

stored blocks. Recent analysis confirms that this block selection phase can consume the majority of total KV retrieval latency [27]. A photonic inner-product engine can break this scaling by performing all N similarity evaluations in parallel, using wavelength multiplexing to avoid the sequential memory access pattern entirely.

We propose PRISM (**P**hotonic **R**anking via **I**nnner-product **S**imilarity with **M**icroring weights), a TFLN photonic similarity engine that realizes the photonic broadcast search concept for KV cache block selection. PRISM encodes the query sketch onto d WDM wavelength channels, broadcasts it to N parallel MRR weight-bank channels via a $1 \times N$ optical splitter, and computes all N similarity scores—each as an analog optical dot product $I_n \propto \sum_j w_{n,j} s_j$ —in $O(1)$ optical latency. A compact electronic top- k comparator selects the highest-scoring block indices, and only the corresponding KV blocks are fetched from memory.

Figure 1 contrasts the conventional electronic full-scan approach with the PRISM photonic block-selection pipeline.

Our contributions are as follows:

- Structural match and photonic broadcast search architecture.** We identify a *structural match* between the KV cache block-selection task and the photonic broadcast-and-weight paradigm: the query fans out identically to all candidates (passive optical splitting), stored signatures are quasi-static (fast MRR electro-optic programming), and only rank order matters (relaxed precision). We propose and analyze a photonic similarity engine that exploits this match, present a complete optical power budget analysis covering splitting loss, MRR insertion loss, and photodetector noise floors, and derive the signal-to-noise ratio (SNR) requirements for reliable top- k ranking (Sec. and Sec.).
- Hardware-aware impairment modeling and NIAH validation.** We build a device-level impairment model incorporating weight quantization (4–8 bits), residual thermal drift, insertion loss chains, photodetector noise, and MRR crosstalk, and show that recall degrades by less than 10% under realistic conditions. End-to-end needle-in-a-haystack (NIAH) evaluation with Qwen2.5-7B demonstrates that MRR-selected block-sparse attention matches full-attention accuracy at context lengths from 4K to **64K tokens** (within the model’s native context window), while replacing the electronic selection with photonic $O(1)$ -latency computation. Beyond 64K, model-intrinsic accuracy degrades independent of block selection (Sec.).
- Photonic scaling analysis.** We derive energy and latency models for PRISM and electronic baselines (GPU full scan, GPU ANN, NVIDIA ICMS), identifying the context-length crossover point above which

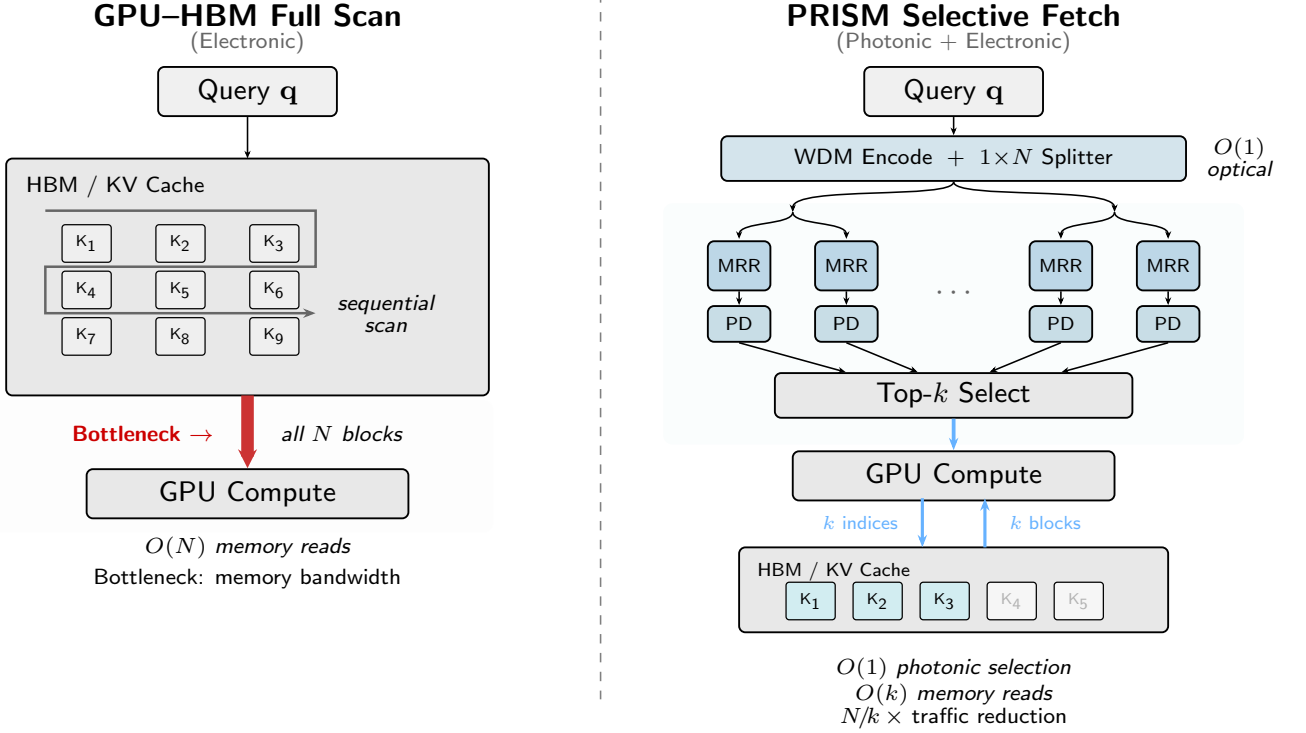


FIG. 1. Conceptual comparison of KV cache access strategies. **Left:** GPU-HBM full scan—the processor sequentially reads all N KV blocks from HBM to compute attention, bottlenecked by memory bandwidth. **Right:** PRISM selective fetch—the query is broadcast optically to all N signature channels in parallel; only the top- k highest-scoring blocks are fetched from memory, reducing traffic by N/k times.

PRISM is favorable, and analyze how the photonic architecture scales to million-token contexts (Sec.).

4. Double-scaling advantage and retrieval head analysis. We systematically profile retrieval-head ratios across Qwen2.5-7B and Qwen3-8B, confirming that over 90% of KV heads are retrieval heads (at threshold $\tau = 0.3$), and reveal a *double-scaling* advantage: as context grows, both the per-head benefit of $O(1)$ photonic computation and the fraction of heads requiring acceleration increase simultaneously. We evaluate block-level signatures, demonstrating that mean-key projection achieves 77.3% recall@8 with $d = 32$ (Sec.).

BACKGROUND

KV Cache in Transformer Inference

The core of modern LLMs is the multi-head self-attention mechanism [28]. Given an input sequence of n tokens embedded as $\mathbf{X} \in \mathbb{R}^{n \times d_{\text{model}}}$, each attention head h in layer ℓ projects the input into queries, keys,

and values:

$$\begin{aligned} \mathbf{Q}^{(\ell,h)} &= \mathbf{X} \mathbf{W}_Q^{(\ell,h)}, \\ \mathbf{K}^{(\ell,h)} &= \mathbf{X} \mathbf{W}_K^{(\ell,h)}, \\ \mathbf{V}^{(\ell,h)} &= \mathbf{X} \mathbf{W}_V^{(\ell,h)}, \end{aligned} \quad (1)$$

where $\mathbf{W}_Q, \mathbf{W}_K, \mathbf{W}_V \in \mathbb{R}^{d_{\text{model}} \times d_h}$ and $d_h = d_{\text{model}}/H$ is the per-head dimension. The attention output is computed as

$$\text{Attn}(\mathbf{Q}, \mathbf{K}, \mathbf{V}) = \text{softmax}\left(\frac{\mathbf{Q}\mathbf{K}^T}{\sqrt{d_h}}\right) \mathbf{V}. \quad (2)$$

During the autoregressive *decode phase*, the model generates one token at a time. At step t , only the new query vector $\mathbf{q}_t \in \mathbb{R}^{d_h}$ is computed, but the attention score requires the inner product of \mathbf{q}_t with all t previously cached key vectors:

$$\alpha_{t,i} = \frac{\mathbf{q}_t \cdot \mathbf{k}_i}{\sqrt{d_h}}, \quad i = 1, \dots, t. \quad (3)$$

The KV cache stores $\mathbf{K}^{(\ell,h)}$ and $\mathbf{V}^{(\ell,h)}$ for all layers and heads, consuming memory

$$M_{\text{KV}} = 2 L H_{\text{KV}} d_h n b_{\text{prec}}, \quad (4)$$

where H_{KV} is the number of KV heads (which equals H for multi-head attention but is reduced under grouped-query attention, GQA [29, 30]) and b_{prec} is the byte width per element (2 for BF16). For Llama-3.1-8B ($L=32$, $H_{KV}=8$ with 4-group GQA, $d_h=128$) at $n = 128\,000$, eq. (4) gives $M_{KV} \approx 16$ GB, which already consumes a substantial fraction of GPU HBM and grows linearly with n .

Crucially, the decode phase is *memory-bandwidth-bound*: each generated token requires reading the entire KV cache but performs only $O(n \cdot d_h)$ multiply-accumulate operations per head. The arithmetic intensity (FLOPs per byte) is $1/(2d_h) \ll 1$, far below the compute-to-bandwidth ratio of modern GPUs (50 FLOP/B to 200 FLOP/B), leaving the compute units idle while waiting for data [1].

Retrieval Heads and Selective Attention

The observation that not all attention heads require the full KV cache was formalized by DuoAttention [19] and RazorAttention [20]. These works define a *retrieval ratio* $R_h^{(\ell,h)}$ for each head as the fraction of attention mass that falls outside a local window of size w :

$$R_h^{(\ell,h)} = 1 - \frac{1}{T} \sum_{t=1}^T \sum_{i=\max(1,t-w)}^t \alpha_{t,i}^{(\ell,h)}, \quad (5)$$

where $\alpha_{t,i}^{(\ell,h)}$ is the attention weight from eq. (3) and T is the total sequence length of a calibration corpus. Heads with $R_h > \tau$ (typically $\tau \approx 0.1$) are classified as *retrieval heads*; the rest are *streaming heads*.

Empirically, DuoAttention identifies approximately 25% (MHA) to 50% (GQA) of heads as retrieval heads via learned gating optimization [19]. Streaming heads can be served with a small sliding-window cache (e.g., $w = 256$), drastically reducing their memory footprint. However, retrieval heads still require access to the full context, making their KV traffic the dominant bottleneck.

Photonic Similarity Engine

As noted in Sec. , the coarse block-selection step is a similarity search whose properties—identical query fan-out, quasi-static weights, and rank-order-only output—make it a natural fit for photonic broadcast-and-weight hardware. We now review the key photonic concepts underlying this match.

Broadcast-and-weight architecture. Tait *et al.* [16, 17] introduced the *broadcast-and-weight* (B&W) paradigm for neuromorphic photonic networks. In this architecture, d input signals are encoded on distinct wavelengths $\lambda_1, \dots, \lambda_d$ and broadcast via a $1 \times N$ optical

splitter to N output channels. Each output channel contains d microring resonators (MRRs), each tuned to one wavelength, whose transmission coefficients serve as programmable weights $w_{n,j}$ for channel n and wavelength j . A wavelength-insensitive photodetector at each output integrates over all wavelengths, yielding the photocurrent:

$$I_n = \mathcal{R} P_0 \sum_{j=1}^d w_{n,j} s_j, \quad (6)$$

where \mathcal{R} is the detector responsivity, P_0 the per-channel optical power after splitting, and s_j the query signal on wavelength λ_j . The photocurrent I_n is thus proportional to the inner product $\mathbf{w}_n \cdot \mathbf{s}$ —precisely the similarity score between stored signature n and the broadcast query. This operation completes in a single optical transit time (~ 10 ps per mm), independent of d and N (up to splitting loss limits).

WDM spectral encoding. The query vector is encoded in the *spectral domain*: each component s_j modulates the optical power on a dedicated wavelength channel λ_j , so the full d -dimensional vector propagates as a single multi-wavelength beam in one waveguide. This spectral encoding is distinct from *spatial encoding*, where each component occupies a separate waveguide, because it enables the key broadcast step—splitting one waveguide into N copies—with no additional multiplexing hardware. Channel spacings of 0.8 nm to 1.6 nm within the C-band support $d = 32$ –128 channels using standard dense WDM (DWDM) laser combs and MRR filter banks.

Comparison with other photonic paradigms. Alternative photonic architectures—MZI meshes [13, 31–33] and coherent processors—require $O(d^2)$ elements or global phase stability, and do not naturally support the one-to-many fan-out needed for similarity search. The broadcast-and-weight paradigm uses incoherent intensity-domain processing, where each MRR operates independently and the photodetector sums power rather than field amplitude, eliminating the need for global phase coherence and making it uniquely suited to the block-selection task.

MRR weight banks. Each output channel employs d microring resonators whose electro-optically tunable transmission implements programmable weights $w \in [0, 1]$. The MRR physics and TFLN-specific device parameters are detailed in Secs. and .

WDM-based matrix-vector multiplication. Scalable MRR weight banks with up to 16 wavelength channels and ~ 7 -bit precision have been demonstrated [34, 35], building on early silicon MRR electro-optic modulators [36], and recent large-scale photonic accelerators validate integration beyond 16 000 components [10, 11, 13, 37].

The key advantage of this photonic approach for the KV cache selection problem is that the “weight matrix”—

the collection of block signatures—is quasi-static and can be programmed into MRR resonances via electro-optic tuning, while the “input vector”—the query sketch—changes at every decode step but is broadcast optically to all N channels simultaneously. This decoupling of weight programming rate from inference rate is what enables the $O(1)$ optical latency scaling that electronic approaches cannot match. While Lightning-Transformer [11] targets full attention computation, PRISM takes a complementary approach: accelerating only the lightweight block-selection ranking task, which requires lower precision and fewer channels, making the photonic implementation more practical.

PHOTONIC RETRIEVAL ARCHITECTURE

System Overview

PRISM is a photonic similarity engine that sits between the KV cache storage (HBM or flash-backed ICMS) and the GPU’s attention compute units. It does not replace any part of the GPU pipeline; rather, it acts as a *photonic broadcast search* module that determines which KV cache blocks should be fetched for each retrieval head at each decode step.

The system operates as a five-stage pipeline, illustrated in fig. 2. For each retrieval head at each decode step:

1. The GPU computes the query vector \mathbf{q}_t and applies the signature projection to obtain a d -dimensional query sketch \mathbf{s}_q .
2. \mathbf{s}_q is converted to the optical domain and broadcast.
3. The photonic weight bank computes N inner products in parallel.
4. Photodetectors produce N analog similarity scores.
5. A digital top- k selector identifies the best blocks, and only those blocks are fetched from KV cache storage.

The GPU then computes exact attention over the selected blocks plus the local sliding window, producing the final attention output.

Signature Encoding

The performance of PRISM depends critically on the quality of the block-level signatures programmed into the MRR weight banks. Since signature encoding defines the input interface between the digital LLM pipeline and the photonic engine, we describe it first. We consider four signature construction methods.

Mean key. The simplest approach averages the key vectors within each block:

$$\sigma_n = \frac{1}{B} \sum_{i \in \text{block } n} \mathbf{k}_i^{(\ell, h)}. \quad (7)$$

This preserves the original key-space geometry but requires d_h -dimensional signatures (e.g., $d_h = 128$), demanding a correspondingly large number of MRRs per channel.

PCA projection. Principal component analysis over the key distribution yields a projection matrix $\mathbf{P} \in \mathbb{R}^{d \times d_h}$ ($d \ll d_h$) that captures the dominant variance directions. The signature becomes $\sigma_n = \mathbf{P} \bar{\mathbf{k}}_n$, reducing the MRR count per channel from d_h to d .

Random projection. The Johnson–Lindenstrauss (JL) lemma guarantees that a random Gaussian matrix $\mathbf{R} \in \mathbb{R}^{d \times d_h}$ with $d = O(\epsilon^{-2} \log N)$ preserves pairwise distances (and hence inner-product rankings) to within a factor $1 \pm \epsilon$ with high probability [38]. The query sketch is computed identically: $\mathbf{s}_q = \mathbf{R} \mathbf{q}_t$. Random projection is attractive because it requires no training and provides worst-case guarantees.

Learned projection. A trainable linear layer $\mathbf{W}_{\text{proj}} \in \mathbb{R}^{d \times d_h}$ is optimized end-to-end to maximize recall@ k on a calibration set. This can outperform random projections when the key distribution has exploitable structure, but requires per-model training.

Balanced photodetection. The add-drop MRR configuration provides both through-port and drop-port outputs simultaneously. A balanced photodetector pair measures the differential photocurrent $I_{\text{bal}} = I_{\text{through}} - I_{\text{drop}}$, yielding a signed weight $w_{n,j} = T_{\text{through}}(\lambda_j) - T_{\text{drop}}(\lambda_j) \in [-1, +1]$. On-resonance (minimum through-port transmission), $w \approx -1$; fully detuned, $w \approx +1$. This eliminates the need for split encoding or ReLU projection, enabling direct signed inner products with d MRRs per channel (half the count of split encoding) while preserving full sign information.

WDM Query Broadcast

The d -dimensional query sketch $\mathbf{s}_q = [s_1, s_2, \dots, s_d]$ is converted from the digital domain by d digital-to-analog converters (DACs), each driving a Mach–Zehnder modulator (MZM) [39] that impresses the value s_i onto wavelength λ_i from a WDM laser comb source. The modulated signals are multiplexed into a single waveguide carrying d wavelength-encoded values [40, 41].

The DAC resolution requirement is modest: since the task is ranking rather than exact computation, 4–6 bits of input precision suffice (Sec.). This relaxation is critical because high-resolution, high-speed DACs are a major energy cost in photonic accelerators. At 4-bit resolution, a DAC operating at 1 GSa/s consumes approximately 0.5 mW per channel.

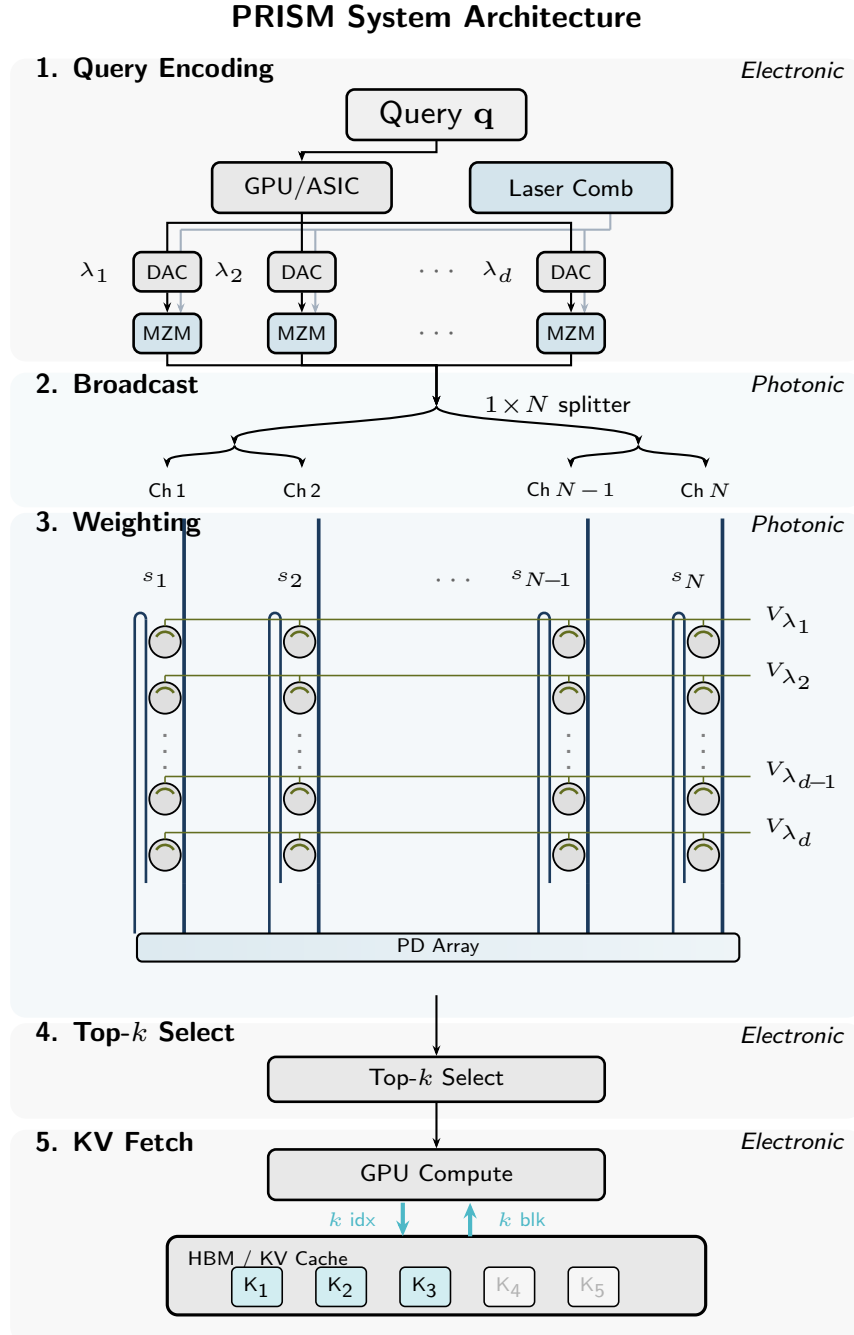


FIG. 2. PRISM system architecture (five-stage pipeline). **Stage 1 (Query Encoding):** The GPU/ASIC computes the query sketch $\mathbf{q} = [q_1, \dots, q_d]$ and encodes each component onto a WDM wavelength via DAC-driven modulators, producing a WDM query signal where $P(\lambda_j) = q_j$. **Stage 2 (Broadcast):** A $1 \times N$ optical splitter distributes identical copies of the d -wavelength signal to all N signature channels (splitting loss: $-10 \log_{10} N$ dB). **Stage 3 (Signature Weighting):** Each channel passes through a row of d MRRs on the TFLN photonic chip; the transmission $t_{ij} = s_{ij}$ of each MRR is electro-optically programmed via DC bias electrodes to encode the block signature weight, performing wavelength-selective multiplication $P_{\text{out}}(\lambda_j) = q_j \times s_{ij}$. **Stage 4 (Summation):** Broadband photodetectors integrate all wavelengths, yielding photocurrents $I_i = \mathcal{R} \cdot \sum_j (q_j \cdot s_{ij})$ that are proportional to the inner product $\mathbf{q} \cdot \mathbf{s}_i$. **Stage 5 (Top- k Selection):** ADCs digitize the N photocurrents, a digital top- k selector identifies the k highest-scoring block indices, and a memory controller fetches only those KV blocks from HBM/flash storage.

Signed query encoding. The WDM intensity encoding $P(\lambda_j) = s_j$ is inherently non-negative. To encode signed query sketches, we apply an offset-bias transformation: $\tilde{s}_j = s_j - s_{\min}$, where $s_{\min} = \min_j s_j$. The shifted values $\tilde{s}_j \geq 0$ are directly encoded as optical powers. At each photodetector, the output becomes $I_n = \mathcal{R} \sum_j w_{n,j} \tilde{s}_j P_0 = \mathcal{R} \sum_j w_{n,j} (s_j - s_{\min}) P_0 = \mathcal{R} P_0 \left[\sum_j w_{n,j} s_j - s_{\min} \sum_j w_{n,j} \right]$. The bias term $s_{\min} \sum_j w_{n,j}$ is identical for all channels sharing the same weight sum and can be digitally subtracted after ADC conversion, or—if only rank ordering matters—simply ignored when $\sum_j w_{n,j}$ is approximately constant across blocks (which holds for normalized signatures). This offset-bias approach requires no additional optical hardware and preserves the $O(1)$ broadcast property.

The multiplexed d -wavelength signal is then split into N copies by a $1 \times N$ optical splitter tree. Each copy carries the full query sketch, attenuated by the splitting loss:

$$L_{\text{split}} = 10 \log_{10}(N) + \alpha_{\text{excess}} \lceil \log_2 N \rceil \quad [\text{dB}], \quad (8)$$

where $\alpha_{\text{excess}} \approx 0.2$ dB per stage for optimized 1×2 directional couplers. For $N = 1024$ blocks, the total splitting loss is approximately 32 dB, requiring a laser source power of 10 dBm to 20 dBm to maintain adequate signal-to-noise ratio (SNR) at the photodetectors.

To manage loss, the N channels can be organized into N_{bank} independent banks, each serving N/N_{bank} channels with a separate splitter tree. This reduces per-bank splitting loss at the cost of additional laser sources or optical amplifiers. The key point is that the broadcast is *passive* (no per-channel energy beyond splitting loss): the same query vector reaches all N channels simultaneously, with no per-channel memory access or data movement.

MRR Weight Bank Similarity Engine

Each of the N output channels contains a linear array of d MRRs, one per wavelength channel. The j -th MRR in channel n is electro-optically tuned so that its transmission at wavelength λ_j encodes the signature weight $w_{n,j}$:

$$\begin{aligned} P_{\text{out},n}(\lambda_j) &= w_{n,j} \cdot P_{\text{in}}(\lambda_j), \\ w_{n,j} &= T_{\text{through},n}(\lambda_j) - T_{\text{drop},n}(\lambda_j) \in [-1, +1]. \end{aligned} \quad (9)$$

The total number of MRRs in the system is $d \times N$. For $d = 64$ and $N = 1024$, this yields 65 536 MRRs—a large but feasible integration scale for current photonic platforms [35].

Weight programming occurs at the block completion rate. When a new KV cache block of B tokens is completed, the corresponding column of MRR weights

is updated via electro-optic (Pockels) tuning with sub-nanosecond response time. During steady-state decoding, the weight bank is static and the only dynamic signal is the broadcast query sketch. Because TFLN EO tuning is capacitive, the MRR weight bank consumes near-zero static power—only switching energy (~ 5 fJ per weight update) is required. This 5 fJ figure refers to the MRR electrode charging energy alone; the total switching energy including CMOS driver circuits is estimated at 50–500 fJ.

Each channel terminates in a broadband (wavelength-insensitive) photodetector [42] that integrates the optical power across all d wavelengths:

$$\begin{aligned} I_n &= \mathcal{R} \sum_{j=1}^d [T_{\text{through},n}(\lambda_j) - T_{\text{drop},n}(\lambda_j)] s_j P_0 \\ &= \mathcal{R} \sum_{j=1}^d w_{n,j} s_j P_0, \end{aligned} \quad (10)$$

where $w_{n,j} \in [-1, +1]$. This is precisely an *analog optical dot product*: the photocurrent $I_n \propto \sum_{j=1}^d w_{n,j} s_j$ computes the similarity score $\mathbf{w}_n \cdot \mathbf{s}_q$ between stored block signature n and the broadcast query [43], with no explicit multiply-accumulate circuit. The physics of broadband photodetection inherently performs the summation—no electronic accumulator is needed [44].

Electronic Top- k Interface

The N photocurrents are converted to digital values by N ADCs and fed to a digital top- k comparator network. The comparator identifies the k channels with the largest similarity scores and outputs their indices. For $k \ll N$, a partial-sort network suffices, with complexity $O(N \log k)$ and latency of a few nanoseconds at 1 GHz clock. The ADC resolution can be as low as 4–6 bits, since only the rank ordering matters.

Device Parameters

Table I summarizes the assumed device parameters for the thin-film lithium niobate (TFLN) photonic platform, based on recent demonstrations of high- Q TFLN micro-ring resonators [45, 46] and MRR weight bank architectures [35, 47]. The physical chip layout for an 8×8 demonstration configuration is shown in fig. 3.

The total MRR count ($d \times N$; eq. (9)) scales with configuration as shown in table VII. Because TFLN electro-optic tuning is capacitive, the static power consumption is near zero (Sec.).

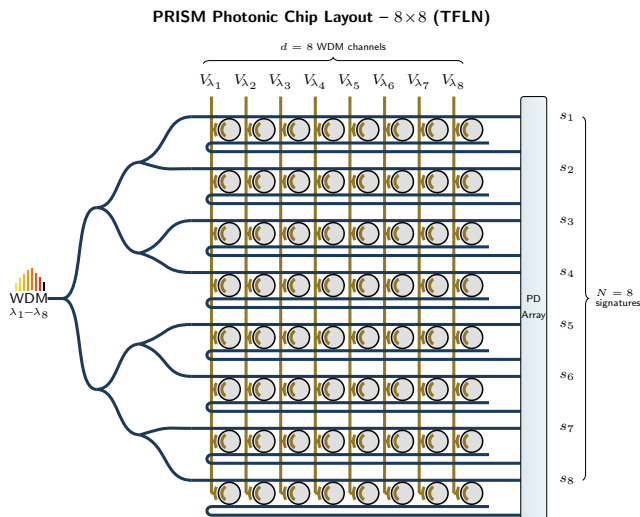


FIG. 3. PRISM photonic chip layout for an 8×8 configuration ($d = 8$ WDM channels, $N = 8$ signature rows). Left: the WDM query input (λ_1 – λ_8) enters and is split by cascaded 1×2 Y-junctions. Center: each row contains d MRRs coupled to a bus waveguide with coupling gap of ~ 200 – 300 nm; EO DC bias electrodes program the MRR resonances to encode signature weights via the Pockels effect. Right: through-port and drop-port outputs route to balanced Ge-on-Si PD pairs (or optionally on-chip integrated photodetectors). Inset: waveguide cross-section showing the TFLN rib waveguide (600 nm LN on SiO_2). Scale bar: $500 \mu\text{m}$. The layout scales to $d = 32$, $N = 256$ by increasing the splitter tree depth and the number of rows.

PHOTONIC HARDWARE ANALYSIS

We now incorporate realistic photonic device impairments into the PRISM simulation and quantify the optical link budget, noise performance, and energy–latency tradeoffs against electronic baselines.

Device Impairment Modeling

We model six impairment sources that degrade the ideal inner-product computation of eq. (6) [49]: (i) weight quantization (4–8 bit DAC precision) [50], (ii) thermal drift of MRR resonance wavelengths ($\sigma_{\text{drift}} = 0.01$ nm to 0.1 nm) [51], (iii) MRR and waveguide insertion loss, (iv) photodetector shot and thermal noise ($\text{NEP} \sim 10$ pW/ $\sqrt{\text{Hz}}$), (v) inter-channel MRR crosstalk (-15 dB to -30 dB isolation), and (vi) input DAC quantization noise. Table II summarizes the parameter ranges used in the hardware simulation. Full impairment models are provided in Supplementary Section S1.

TABLE I. PRISM device parameters (TFLN platform).

Parameter	Value	Notes
Platform	X-cut TFLN	600 nm LN/ SiO_2
Waveguide	Rib, $1.4 \times 0.6 \mu\text{m}$	500 nm etch
MRR radius	$20 \mu\text{m}$	FSR ≈ 8.3 nm
Q_L	$\sim 10^4$ [‡]	FDTD: 12,500
Extinction	>15 dB	Add-drop
Wt. precision	5 bit	EO resolution
Tuning	EO (Pockels)	28.5 pm/V
Static power	~ 0	Capacitive EO
Switch energy	~ 5 fJ/ring	Per update
Tuning speed	<1 ns	EO response
Modulator	TFLN MZM	$V_\pi L \sim 2$ V·cm
Photodetector	Balanced PD	Differential
WDM ch.	$d = 32$ – 128	1.6 nm spacing [†]
Laser	Comb source	≤ 100 mW

[‡] The FDTD-simulated $Q_L = 12,500$ is limited by mesh discretization, not by material or design physics. Published TFLN micro-ring resonators achieve intrinsic $Q_i \geq 10^6$ – 10^8 [45, 46]; at $Q_i = 10^6$, the loaded Q_L would rise to $\sim 25,000$, improving weight precision and extinction ratio. Higher Q strictly improves PRISM performance; the $Q = 10^4$ design point used here is therefore conservative. See Park & Park [48] for a detailed analysis of FDTD resolution limits and projected high- Q operating regimes.

[†] $d = 32$ – 64 is realistic with current C+L band technology; $d = 128$ requires C+L+S band operation and has not been experimentally demonstrated.

Optical Link Budget

A critical question for any photonic accelerator is whether sufficient optical signal-to-noise ratio (SNR) can be maintained across the complete optical path [33]. The complete optical link budget is provided in Supplementary table S1. For the nominal $d = 32$, $N = 256$ configuration with $P_{\text{laser}} = 20$ dBm, the per-detector received power is -15.9 dBm ($25.7 \mu\text{W}$).

Balanced detection link budget. The link budget in Supplementary table S1 traces the drop-port path to the target photodetector. In the balanced configuration used by PRISM, each MRR channel requires *two* optical paths—through-port and drop-port—each terminated by a separate photodetector and TIA. The through-port path sees lower loss (no drop-port penalty), so the drop-port budget above represents the worst case. Consequently, balanced detection doubles the photodetector and TIA count to $2N$ per wavelength channel; this overhead is reflected in table III.

At $P_{\text{PD}} = -15.9$ dBm $\approx 25.7 \mu\text{W}$ per detector, the resulting photocurrent is $I_{\text{ph}} = \mathcal{R} \cdot P_{\text{PD}} = 1.0 \times 25.7 \mu\text{W} = 25.7 \mu\text{A}$. The electrical SNR at the detector is

$$\text{SNR} = \frac{I_{\text{ph}}^2}{2eI_{\text{ph}}\Delta f + 4k_B T \Delta f / R_L + (\mathcal{R} \cdot \text{NEP})^2 \Delta f}, \quad (11)$$

where $\Delta f \approx 1$ GHz (matching the query update rate)

and $\text{NEP} = 10 \text{ pW}/\sqrt{\text{Hz}}$ (eq. (S5)). For $R_L = 1 \text{ k}\Omega$ and $T = 300 \text{ K}$, we obtain $\text{SNR} \approx 37.2 \text{ dB}$ —well above the minimum required for reliable rank ordering [52]. (Note: $R_L = 1 \text{ k}\Omega$ assumes a transimpedance amplifier (TIA) front-end rather than 50Ω termination.)

For larger bank sizes ($N = 1024$), the additional 6 dB splitting loss reduces the per-detector power to $-21.9 \text{ dBm} \approx 6.5 \mu\text{W}$, yielding $\text{SNR} \approx 25.5 \text{ dB}$. This remains adequate for top- k ranking, as verified by the recall analysis in Sec. . Beyond $N = 4096$ ($\text{SNR} \approx 13.5 \text{ dB}$), the link budget requires either a higher-power laser ($P_{\text{laser}} > 26 \text{ dBm}$) or the banked splitter architecture described in Sec. .

Figure 4 illustrates the per-detector received power and SNR as a function of the bank size N , clearly showing the crossover point at which banked architectures or optical amplification become necessary.

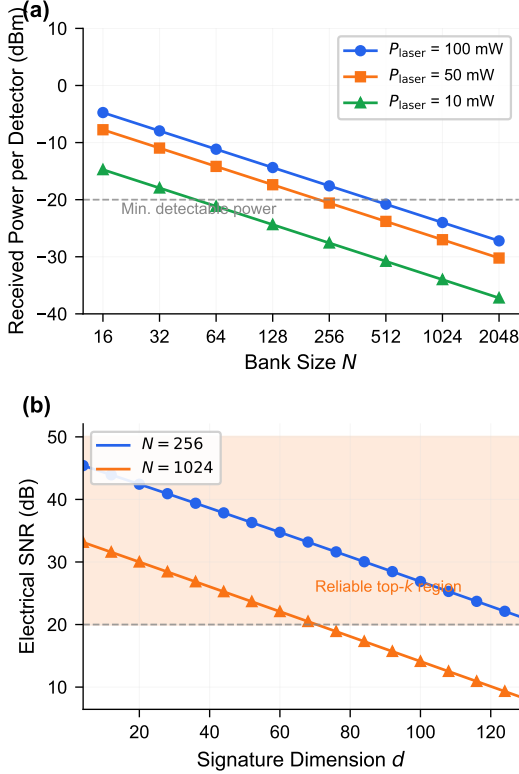


FIG. 4. Optical power budget analysis. (a) Per-detector received power vs. bank size N for three laser powers. The horizontal dashed line indicates the minimum detectable power (-20 dBm). (b) Electrical SNR at the photodetector vs. signature dimension d for $N = 256$ and $N = 1024$. The shaded region marks $\text{SNR} > 20 \text{ dB}$, sufficient for reliable top- k ranking.

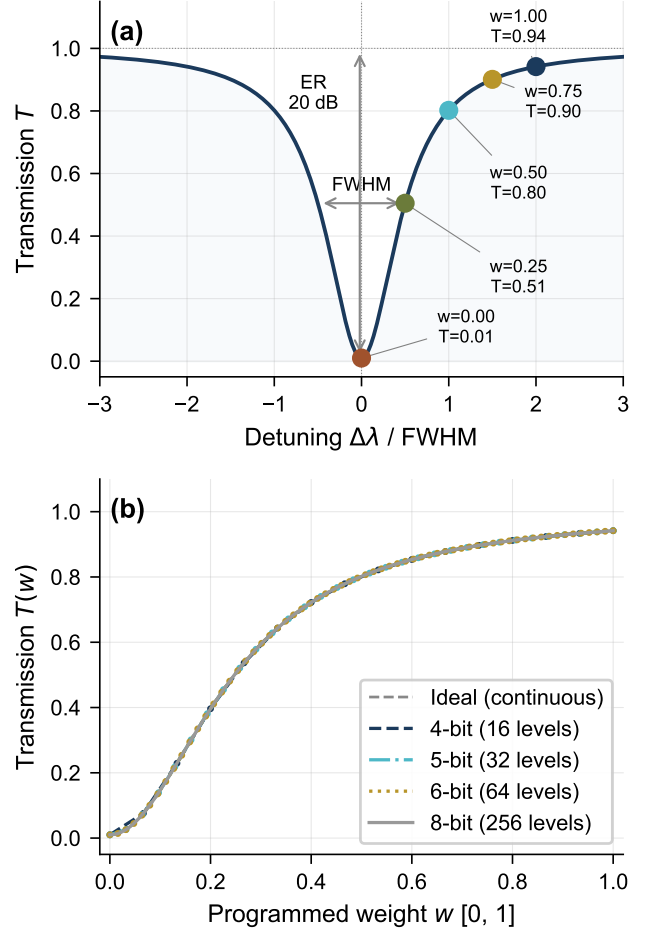


FIG. 5. MRR weight encoding principle. (a) Throughport and drop-port transmission of a single add-drop MRR ($Q_L = 10,000$, $\text{ER} = 20 \text{ dB}$). The balanced weight $w = T_{\text{through}} - T_{\text{drop}}$ maps from -1 (on-resonance) to $+1$ (fully detuned). (b) Weight-to-balanced-transmission mapping for different DAC precisions.

TABLE II. Device impairment parameter ranges used in hardware simulation.

Impairment	Parameter	Range
Weight quantization	b (bits)	4–8
Thermal drift	σ_{drift} (pm)	10–100
MRR insertion loss	IL_{MRR} (dB)	0.02–0.05 ^c
Splitter excess loss	α_{excess} (dB/stage)	0.1–0.3
Detector NEP	($\text{pW}/\sqrt{\text{Hz}}$)	1–20
MRR crosstalk	Isolation (dB)	-15 to -30
DAC resolution	b_{DAC} (bits)	4–8

^c Through-port IL per non-target MRR; drop-port (target MRR) IL is $\sim 0.1 \text{ dB}$.

Recall Degradation Analysis

We inject impairments into the inner-product computation and measure recall@ k degradation relative to the

ideal (floating-point) baseline. Individual impairment sweeps (quantization precision, thermal drift, weight fidelity, and detector noise) are presented in Supplementary Figs. S1–S4.

Combined impairments. We simulate the full impairment chain (quantization + drift + loss + noise + crosstalk) using a Monte Carlo approach with 100 trials of 500 blocks ($d = 32$). Figure 6 visualises the effect for a single trial: the MRR scores correlate strongly with the digital baseline ($\rho > 0.98$), and the top- k ranking is largely preserved. Figure 7 maps the recall degradation as a function of both weight precision and thermal drift magnitude, identifying the operating region in which Recall@8 exceeds 80%.

The combined recall degradation at $b = 6$, $\sigma_{\text{th}} = 0.01$, and $\sigma_{\text{det}} = 0.01$ is approximately 8%, yielding an effective Recall@8 of 0.916 ± 0.087 (vs. 1.000 ideal). Each impairment source individually contributes modestly (5-bit quantization: 0.904, drift: 0.948, noise: 0.928), but their combination remains above the 90% threshold required for effective block selection.

The recall degradation results establish the acceptable operating region for the MRR weight bank. End-to-end NIAH validation with MRR-simulated block selection, confirming that these impairments do not degrade downstream task accuracy, is presented in Sec. .

Energy Model

Table III breaks down the energy per query evaluation for the PRISM system. We define the energy metric as the total energy consumed by the photonic pipeline to evaluate all N blocks simultaneously for a single query on a single KV head (i.e., one complete selection operation).

A key advantage of the TFLN platform is the elimination of static MRR tuning power. TFLN electro-optic tuning via the Pockels effect is capacitive and consumes near-zero static power (see Sec. for the quantitative SOI comparison). The only energy cost per weight update is the switching energy of ~ 5 fJ per ring, which is negligible compared to the dynamic optical and electronic components [40]. Note that while the total system power (~ 1.25 W) is dominated by the TEC, this is a fixed overhead independent of query rate. At a throughput of T head-queries per second, the amortized TEC contribution is $1/T$ joules per head-query. For $T = 10^5$ (e.g., 100 concurrent users \times 1000 tokens/s), TEC adds ~ 10 μ J per head-query—still well below the GPU baseline.

For comparison, the H100 GPU full-scan baseline reads every KV block signature once per query per head. The energy per selection is

$$\begin{aligned} E_{\text{scan}} &= 2 d_h N b_{\text{prec}} E_{\text{byte}} \\ &= 2 \times 128 \times 1024 \times 2 \times 31 \text{ pJ/B} \quad (12) \\ &\approx 16.3 \mu\text{J}, \end{aligned}$$

where $d_h=128$ is the head dimension, $N=n/B=1024$ blocks at 128K context ($B=128$), $b_{\text{prec}}=2$ B (bf16), and $E_{\text{byte}} \approx 31$ pJ/B (≈ 3.9 pJ/bit, standard HBM3 specification) [53]. Note that this baseline assumes GPU scans the full key dimension $d_h=128$; if the GPU instead scans compressed $d=32$ signatures, the energy reduces to ~ 4.1 μ J ($4\times$ lower). Even in this fairer comparison, PRISM’s ~ 2290 pJ selection energy remains $\sim 1800\times$ below the GPU scan [44]. GPU ANN (FAISS IVF-PQ) reduces the full-key scan to ~ 5 μ J by scanning $O(\sqrt{N})$ centroids. NVIDIA ICMS consumes ~ 10 μ J, estimated by replacing BW_{HBM} with the DPU’s internal LPDDR5 bandwidth (~ 100 GB/s) and assuming a similar scan pattern over the flash-backed KV index.

Latency Model

The latency breakdown (Supplementary table S2) shows a total photonic pipeline latency of ~ 9 ns, dominated by the CMOS top- k sorting logic (5 ns) and TIA+ADC conversion (2 ns).

The total PRISM latency of ~ 9 ns compares favorably with the electronic baselines: GPU full scan ~ 5 μ s, GPU ANN ~ 1 μ s, and NVIDIA ICMS ~ 0.5 μ s—representing a $\sim 500\times$ speedup over full scan. However, this comparison must account for the additional latency of fetching the selected KV blocks from memory after PRISM selection, which adds 0.5 μ s to 2 μ s depending on the memory tier (HBM vs. flash). The net latency benefit of PRISM is therefore most pronounced when the selection ratio k/N is small and the KV cache resides in a slow memory tier (e.g., flash in ICMS). The crossover analysis quantifying these trade-offs across context lengths and baselines is presented in Sec. .

Figure 8 summarises the interplay between signature dimension, photodetector SNR, and ranking accuracy across the operating envelope of PRISM.

Balanced photodetection noise. In the balanced configuration, each channel uses two photodetectors measuring through-port and drop-port signals independently [47]. Shot noise from both PDs adds in quadrature: $\sigma_I^2 = 2e(I_{\text{through}} + I_{\text{drop}})\Delta f$. Since $I_{\text{through}} + I_{\text{drop}} = \mathcal{R}P_0$ (power conservation), the total shot noise is weight-independent, simplifying the noise analysis. The factor of $\sqrt{2}$ increase in noise is offset by the doubled signal dynamic range ($[-1, +1]$ vs $[0, 1]$).

SYSTEM-LEVEL EVALUATION

This section evaluates the complete PRISM pipeline from algorithmic profiling through end-to-end validation. We first profile retrieval heads across two LLM families (Sec.), then evaluate block signature design and recall

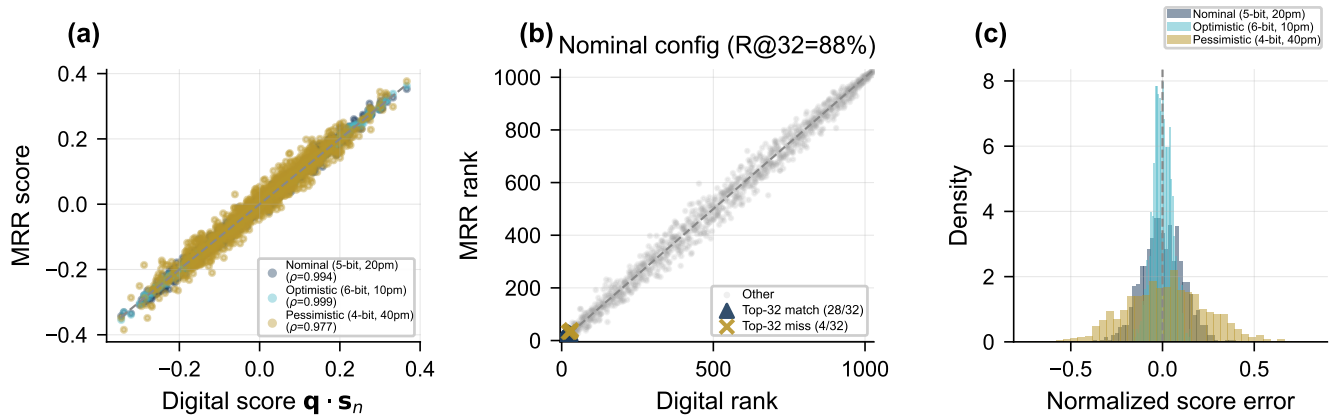


FIG. 6. Digital vs. MRR photonic inner-product comparison ($d = 32$, $N = 256$, $K = 8$). (a) Score correlation between exact (FP64) and MRR-computed similarity for three hardware configurations. Pearson correlation $\rho > 0.98$ for all configs. (b) Rank agreement for the nominal config (5-bit, 20 pm): green triangles indicate correctly identified top- K blocks (7/8 match, Recall@8 = 88%). (c) Normalised score error distributions; pessimistic config (4-bit, 30 pm) shows wider tails but remains zero-centred.

TABLE III. PRISM energy breakdown per query—all $N = 1024$ blocks evaluated simultaneously ($d = 64$, $k = 32$, TFLN platform).

Component	Power (mW)	Energy/query (pJ)
Laser source	100.0	900
TEC (thermal stab.)	1000	9000 [†]
Voltage driver array	5.0	45
DACs (d channels)	32.0	288
MZM modulators	6.4	58
EO bias (static)	~0	~0*
Photodetectors ($2N$, balanced)	10.0	90
TIAs + ADCs ($2N$, balanced)	100.0	900
Top- k logic	1.0	9
Dynamic subtotal	254.4	2290
Total (incl. TEC)	1254.4	11290

*TFLN EO tuning is capacitive; switching energy ~ 5 fJ/ring. [†]The 1 W TEC is a fixed overhead. At throughput T head-queries/s, TEC adds $1/T$ J per head-query (e.g., $T=10^5$: ~ 10 μ J per head-query).

(Sec.), and validate downstream accuracy via Needle-in-a-Haystack experiments with MRR-simulated block selection (Sec.).

Retrieval-Head Analysis

Models and datasets. We profile two representative open-weight LLMs: Qwen2.5-7B-Instruct [54] ($L = 28$, $H = 28$, $d_h = 128$, GQA [29] with $H_{KV} = 4$; total 112 KV heads) and Qwen3-8B [55] ($L = 36$, $H = 32$, $d_h = 128$, GQA with $H_{KV} = 8$; total 288 KV heads). Qwen2.5-7B supports context lengths of at least 128 000 tokens; Qwen3-8B supports up to 32 000 tokens. We compute retrieval ratios $R_h^{(\ell, h)}$ (eq. (5)) on a calibration set of 2–3 random token sequences per context length, with $w = 256$ as the local window size. The retrieval

ratio is measured using a two-step procedure: SDPA-based prefill followed by eager last-token attention extraction. All experiments are run on an NVIDIA RTX 5880 (48 GB VRAM) for bf16 models, and an NVIDIA RTX 5070 (12 GB) for 4-bit quantized variants. We additionally verify consistency between bf16 and 4-bit quantized Qwen2.5-7B, finding that quantization does not substantially alter retrieval head identification (e.g., 91.1% vs. 92.0% at 8K context for bf16 and 4-bit, respectively).

Results. Figure 9 shows the retrieval ratio heatmap across all layers and heads for both models.

Detailed per-context retrieval ratios are provided in Supplementary table S3.

Figure 10 visualizes the retrieval head fraction and mean retrieval ratio as a function of context length.

We observe the following patterns:

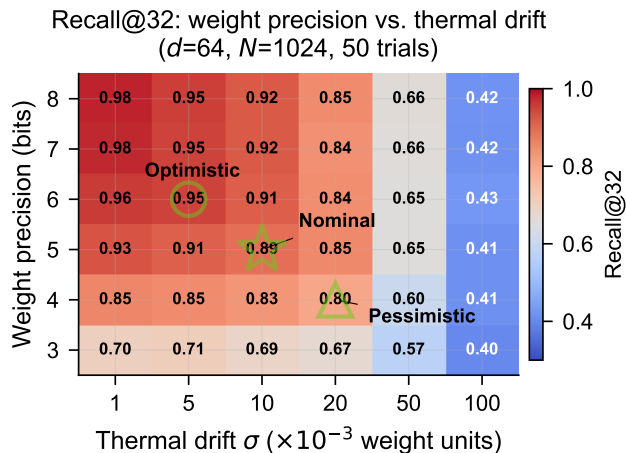


FIG. 7. Combined impairment sensitivity: Recall@8 as a function of weight precision (bits) and thermal drift σ ($d = 32$, $N = 500$, 50 Monte Carlo trials per cell). Markers indicate the three operating points studied in this work: nominal (5-bit, $\sigma = 0.01$), optimistic (6-bit, $\sigma = 0.005$), and pessimistic (4-bit, $\sigma = 0.02$). Recall exceeds 80% for ≥ 5 -bit precision and $\sigma \leq 0.02$.

- Ubiquity of retrieval behavior.** At a threshold of $\tau = 0.3$, 91.1% of KV heads in Qwen2.5-7B and 89.6% in Qwen3-8B are retrieval heads at 8K context. This prevalence increases with context length: for Qwen2.5-7B, the fraction rises from 83.9% at 2K to 98.2% at 128K context, indicating that nearly all heads engage in long-range retrieval at long contexts. This monotonic increase creates a *compounding* advantage for photonic acceleration: not only does the per-head benefit of $O(1)$ photonic computation grow with context, but the fraction of heads requiring acceleration also increases. Note that at the more permissive $\tau = 0.1$ threshold used in [19], essentially 100% of heads qualify as retrieval heads. The reported fraction is thus sensitive to the threshold choice: varying τ from 0.1 to 0.3 shifts the classified fraction from $\sim 100\%$ to $\sim 90\%$. The contrast with DuoAttention’s 25–50% retrieval fraction reflects both (i) different models (Llama-2/Mistral vs. Qwen) and (ii) DuoAttention’s use of a learned gating function optimized on calibration data, which imposes a stricter criterion than a simple threshold on attention mass. In practice, the threshold can be tuned per deployment scenario to trade off between the number of heads served photonically and the complexity of the photonic accelerator.

- Layer distribution.** The highest-scoring retrieval heads are concentrated in layers 14–26, with peak retrieval ratios exceeding 0.93.
- GQA effect.** Because GQA shares KV heads across multiple query heads, the number of *KV cache entries* requiring retrieval-style treatment is even smaller than

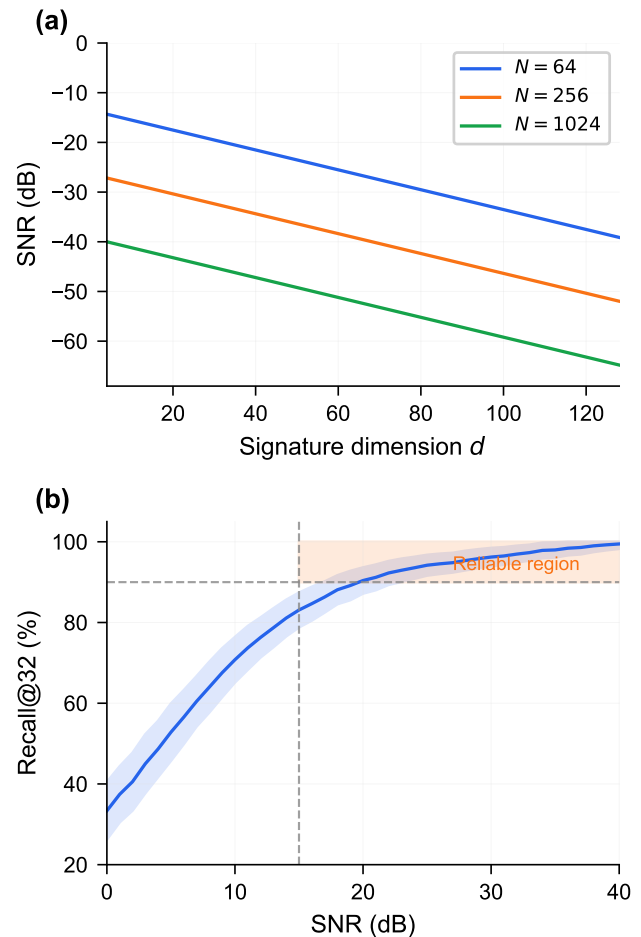


FIG. 8. SNR and recall analysis. (a) Electrical SNR at the photodetector as a function of signature dimension d for three bank sizes. (b) Recall@8 vs. SNR showing that reliable top- k selection ($> 90\%$ recall) requires $\text{SNR} \gtrsim 15$ dB.

the head count suggests.

The key implication for PRISM is that the photonic accelerator needs to serve the vast majority of KV heads—102 out of 112 for Qwen2.5-7B and 258 out of 288 for Qwen3-8B at 8K context. However, GQA sharing means each KV head serves multiple query heads, so the *number of independent weight bank instances* required equals the KV head count, not the query head count.

Block Signature Design

We partition the KV cache into contiguous blocks of B tokens and compute a d -dimensional signature for each block [56]. We evaluate mean-key and random projection signature methods from Sec. at block size $B = 128$ and signature dimensions $d \in \{16, 32, 64, 128\}$, using Qwen2.5-7B at context length $n = 4096$. Our experiments identify $B = 128$ with $d = 32$ and mean-key pro-

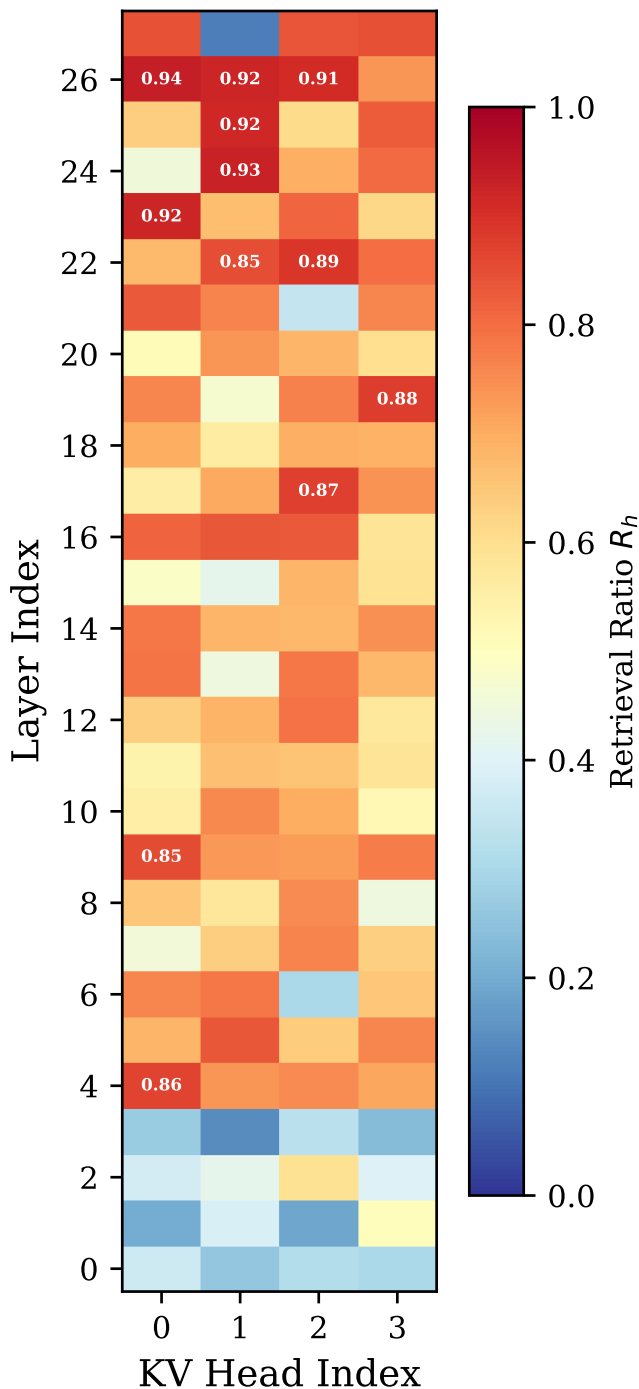


FIG. 9. Retrieval ratio $R_h^{(\ell,h)}$ for each KV head across all layers. Heads with $R_h > 0.3$ (dashed line) are classified as retrieval heads. (a) Qwen2.5-7B: 102/112 heads are retrieval heads (91.1%) at 8K context. (b) Qwen3-8B: 258/288 heads are retrieval heads (89.6%) at 8K context.

jection as the best configuration. At the primary operating point $k=32$, table IV shows $R@32 = 100\%$ at 8K context ($B=128$, 64 blocks), confirming that the signature ranking correctly identifies all relevant blocks. At

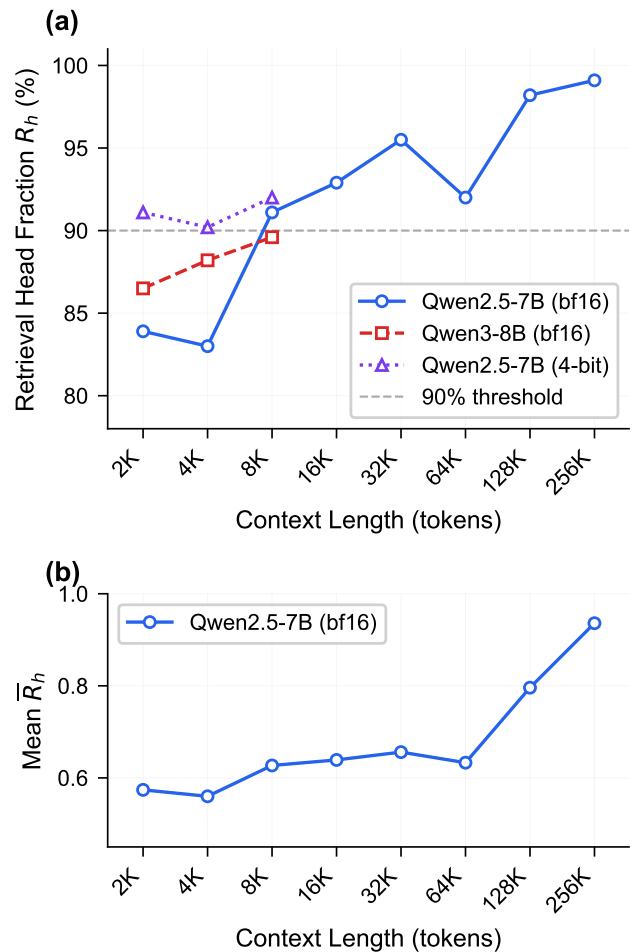


FIG. 10. Retrieval head statistics vs. context length. (a) Retrieval head fraction R_h ($\tau=0.3$) for Qwen2.5-7B (bf16 and 4-bit) and Qwen3-8B (bf16). The fraction exceeds 90% for $n \geq 8K$ and approaches 99% at 256K context. (b) Mean retrieval ratio \bar{R}_h for Qwen2.5-7B (bf16), showing that individual-head retrieval strength also increases with context length.

16K, $R@32$ drops to 57.5%, yet downstream NIAH accuracy remains 100% (table VI), indicating that task-critical blocks are consistently ranked in the top- k even when overall recall is imperfect. This significant gap between block-level recall and task accuracy demonstrates an inherent error tolerance: task-relevant information is distributed across neighboring blocks, providing natural redundancy that absorbs photonic impairment noise. As a stress-test analysis at $k=8$, $R@8 = 77.3\%$ ($R@2 = 31.3\%$, $R@4 = 50.0\%$), confirming that useful ranking signal persists even under aggressively small selection budgets. Mean-key projection consistently outperforms random projection across all tested dimensions, confirming that the natural key-space geometry contains exploitable structure for block ranking.

Why mean-key and random projections? We focus on mean-key and random projection signatures because they

are model-agnostic and require no training, matching our goal of a general-purpose photonic hardware interface. Learned projections (e.g., trained linear maps optimized for recall) could improve signature quality but would require per-model fine-tuning and hardware-aware training, which we leave to future work (Sec.).

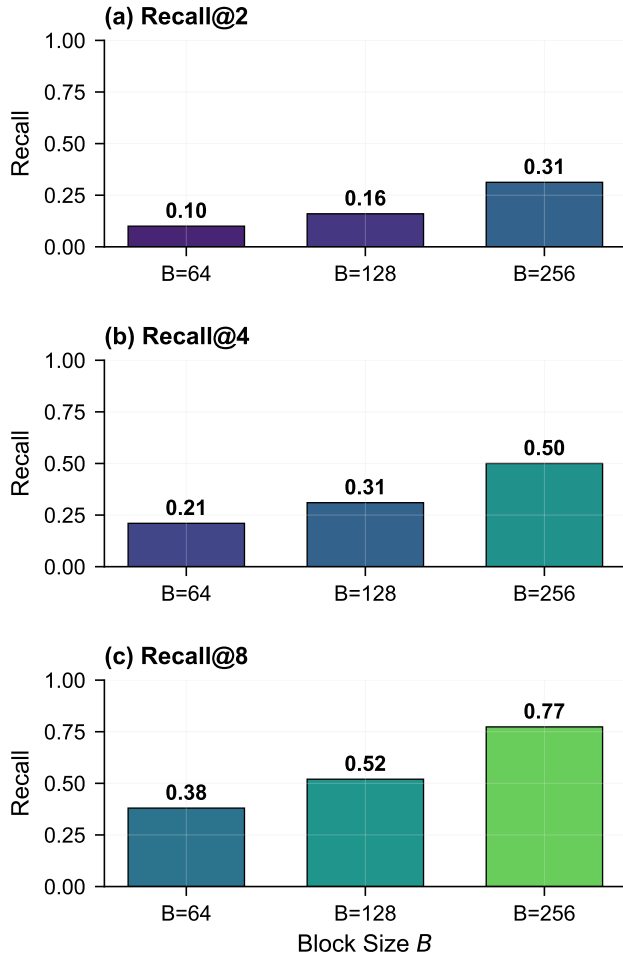


FIG. 11. Recall@ k as a function of signature dimension d for different signature methods. Block size $B = 128$, $k = 8$ (stress-test setting). Mean-key projection consistently outperforms random projection, achieving 77.3% recall@8 at $d = 32$. At the primary operating point $k=32$, recall reaches 100% at 8K context (table IV).

Signed weight encoding. The add-drop MRR configuration with balanced photodetection enables direct encoding of signed weights $w \in [-1, +1]$, eliminating the non-negative constraint of through-port-only architectures. Compared to ReLU projection (which discards sign information, losing $\sim 50\%$ of the signature variance for zero-mean Gaussian signatures), balanced photodetection preserves the full signed inner product. Our simulations show that signed encoding improves Recall@8 by $\sim 87\%$ relative to ReLU projection at $d = 32$ (Supplementary fig. S6).

Recall metric. We define recall@ k [57] as the fraction of the true top- k blocks (by exact query-key inner product) that appear in the PRISM-selected top- k blocks:

$$\text{Recall@}k = \frac{|\mathcal{S}_{\text{PRISM}} \cap \mathcal{S}_{\text{exact}}|}{k}, \quad (13)$$

where $\mathcal{S}_{\text{PRISM}}$ and $\mathcal{S}_{\text{exact}}$ are the sets of top- k block indices selected by PRISM and by exact computation, respectively.

TABLE IV. Recall@ k for PRISM block selection across context lengths. Qwen2.5-7B, $B=128$, $d=32$, mean-key projection. Values averaged over 15 (layer, head) pairs.

n	Blocks	R@8 (%)	R@16 (%)	R@32 (%)	NIAH (%)
4K	16	46.7	100	—*	100
8K	32	29.2	55.8	100	100
16K	64	26.7	41.7	57.5	100
32K	128		(OOM [†])		100
64K	256		—		100

*Only 16 blocks at 4K; $k=32$ exceeds total.

[†]Eager attention OOM at 32K; NIAH uses SDPA (no attention matrix).

Traffic reduction. At the primary operating point $k=32$, the traffic ratio is $kB/n = 32 \times 128/n$. At 128K tokens ($N=1024$ blocks), PRISM selects $k=32$ of $N=1024$ blocks, yielding a $N/k = 1024/32 = 32 \times$ traffic reduction (3.1% traffic). At 1M tokens ($N \approx 7812$ blocks), the reduction grows to $N/k \approx 7812/32 \approx 244 \times$ (0.41% traffic), though model accuracy at such lengths remains model-dependent. Under the stress-test setting $k=8$, the reduction reaches $128 \times$ at 128K and projects to $\sim 977 \times$ at 1M tokens (fig. 12).

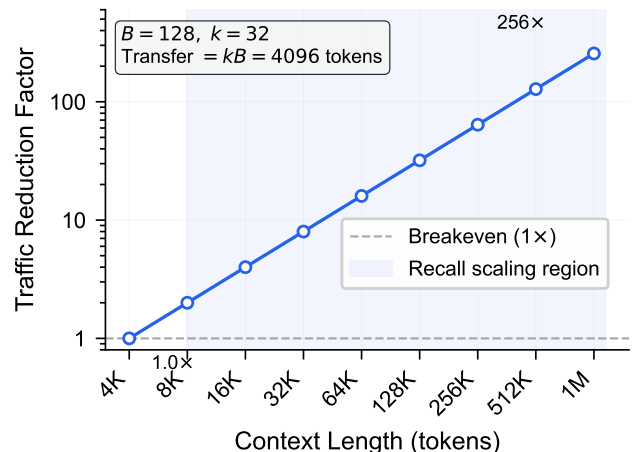


FIG. 12. Memory traffic reduction factor as a function of context length for fixed block size $B = 128$ and $k = 8$ selected blocks. The traffic reduction scales linearly with context length, reaching $977 \times$ at $n = 1\,000\,000$.

NIAH Accuracy Under Hardware Impairments

To validate that the MRR-impaired block selection preserves end-to-end language model performance, we integrate the MRR array simulator into Qwen2.5-7B [54] and evaluate on the Needle-in-a-Haystack (NIAH) benchmark [18, 58].

For each decode step, block signatures (mean-key, $d = 32$) are processed through the MRR simulator to select the top- k blocks. Retrieval heads ($R_h > 0.3$; Supplementary table S3) use MRR-selected blocks plus a 256-token recent window; streaming heads retain full attention. We test four MRR configurations: (i) ideal (floating-point inner product), (ii) 5-bit/20 pm drift (nominal), (iii) 4-bit/30 pm drift (pessimistic), and (iv) 5-bit/10 pm drift (optimistic).

TABLE V. NIAH accuracy (%) with MRR-integrated block selection (Qwen2.5-7B, 11 positions, $k = 8$ stress-test setting).

Configuration	2K	4K	8K
Full attention	90.9	100.0	100.0
Ideal select	90.9	100.0	100.0
5-bit, 20 pm	90.9	100.0	100.0
4-bit, 30 pm	90.9	100.0	100.0
5-bit, 10 pm	90.9	100.0	100.0

Table V shows that all four MRR configurations—including the worst-case 4-bit quantization with 30 pm thermal drift—achieve *identical* NIAH accuracy to full attention at all tested context lengths. The single miss at 2K context (position 50%) is a model-level artifact unrelated to block selection. These results demonstrate that the MRR impairments modelled in Sec. do not degrade downstream task accuracy for the block-selection ranking task.

To validate PRISM across a wide range of context lengths, we extend the evaluation using SDPA-based attention (Flash Attention) with KV cache offloading to CPU RAM via `OffloadedCache`. This enables experiments at context lengths from 4K to 128K on a single GPU (RTX 5880, 48 GB) with 128 GB system RAM. We note that Qwen2.5-7B’s native context window is 128K tokens; at 128K, the base model’s own accuracy degrades to 45.5% on NIAH (table VI), limiting meaningful evaluation beyond 64K. Extrapolation to longer contexts (e.g., 1M tokens via YaRN [7] rope scaling) is technically feasible for the photonic hardware, but model-level accuracy at such lengths remains an open challenge independent of block selection.

For sparse evaluation, we employ *physical token selection*: rather than re-attending to all tokens with a mask, only the tokens from the top- k selected blocks and a recent window are assembled into a compact input (~ 5 K tokens), preserving positional encoding via explicit `position_ids`. This approach mirrors the actual deploy-

ment scenario where only selected KV blocks are fetched from memory.

Table VI presents the extended NIAH results across context lengths from 4K to 128K. The full 2D NIAH heatmap (context length \times needle depth, 10 positions per context) is shown in Supplementary fig. S5. At $k=32$ blocks ($B=128$), all MRR configurations achieve **100% accuracy from 4K through 64K**, perfectly matching full attention. At 128K, the base model itself degrades to 45.5%—a known limitation of Qwen2.5-7B’s context window—making sparse-vs-full comparison uninformative at this length. Within the model’s reliable operating range ($N \leq 64$ K), MRR block selection introduces *zero* accuracy penalty while reducing KV memory traffic by $16\times$ at 64K ($k \cdot B/n = 32 \times 128/65536 = 6.25\%$); the reduction grows to $32\times$ (3.1%) at 128K.

TABLE VI. Extended NIAH accuracy (%) with MRR block selection (Qwen2.5-7B, $B=128$, $d=32$, $k=32$). At 128K the base model degrades (\dagger). *50 needle positions; others use 10 positions.

Configuration	4K*	8K*	16K	32K	64K	128K [†]
Full attention	100	100	100	100	100	45.5
Ideal ($k=32$)	100	100	100	100	100	18.2 [‡]
5-bit, 20 pm	100	100	100	100	100	27.3 [‡]
4-bit, 30 pm	100	100	100	100	100	27.3 [‡]
5-bit, 10 pm	100	100	100	100	100	27.3 [‡]
<i>Needle block recall (MRR top-k selection):</i>						
5-bit, 20 pm	100*	88*	—	—	—	—

*Extended to 50 needle positions (vs. 10 for other columns), confirming robustness of the 10-position findings. Needle block recall at 8K (88%) indicates 6 of 50 needle blocks fall outside the top- $k=32$ selection, yet NIAH answer accuracy remains 100% because surrounding context blocks contain sufficient retrieval cues.

[‡]At 128K, full attention itself degrades to 45.5%; the apparent superiority of impaired configurations over ideal is within sampling noise and is not statistically significant.

PHOTONIC SCALING ANALYSIS

We now analyze how the photonic engine scales to larger systems, identifying constraints from WDM channel density, thermal power, chip area, and time-multiplexed operation.

MRR Integration Scaling

The total MRR count in the PRISM weight bank is

$$N_{\text{MRR}} = d \times N, \quad (14)$$

where d is the number of WDM wavelength channels (signature dimension) and N is the number of parallel sig-

nature banks (one per KV cache block). For a context length of n tokens with block size B , $N = n/B$.

Table VII lists representative configurations spanning three orders of magnitude in MRR count.

TABLE VII. MRR count for representative PRISM configurations. The rightmost column indicates the approximate context length supported at block size $B = 128$.

d	N	N_{MRR}	Context	Feasibility
32	256	8192	32K	Current TFLN
64	1024	65 536	128K	Near-term
128	4096	524 288	512K	Multi-chip

Current photonic integration supports 10^4 – 10^5 active devices per die [35, 59], placing the $d=32$, $N=256$ configuration within demonstrated capability and $d=64$, $N=1024$ at the near-term frontier. The $d=128$, $N=4096$ configuration exceeds single-chip density, requiring chiplet-based multi-chip modules [60] (Sec.).

Thermal Power Budget and WDM Channel Limits

On thermo-optic SOI platforms [51], each MRR requires ~ 2.5 mW of static heater power, yielding aggregate budgets of 20 W ($d=32$, $N=256$) to 164 W ($d=64$, $N=1024$)—approaching the ~ 200 W practical limit with active cooling. On the TFLN platform, MRR tuning via the Pockels effect ($r_{33} = 30.9$ pm/V) is capacitive with near-zero static power (< 1 μ W per ring from CMOS driver leakage):

$$P_{\text{static}}^{\text{TFLN}} = d \times N \times P_{\text{leakage}} < d \times N \times 1 \mu\text{W}. \quad (15)$$

For the $d=64$, $N=1024$ configuration, $P_{\text{static}} < 0.07$ W—a $\sim 2400\times$ reduction over SOI. The switching energy (~ 5 fJ per ring) yields < 0.3 μ W total switching power at typical decode rates—negligible. Residual thermal stabilization via TEC (~ 1 W for a ~ 1 cm² chip) remains necessary but is orders of magnitude below SOI heater budgets. TFLN’s lower thermo-optic coefficient ($dn/dT \approx 4 \times 10^{-5}$ K⁻¹ vs. 1.8×10^{-4} K⁻¹ for Si) further reduces thermal crosstalk.

WDM channel limits. The signature dimension d is constrained by the MRR free spectral range (FSR) [61]. A single-FSR MRR ($R = 20$ μ m, $\text{FSR} \approx 8.3$ nm) supports only ~ 5 channels at 200 GHz spacing. Vernier-coupled dual-ring filters extend the effective FSR to ~ 50 nm ($d \sim 30$); C+L band operation (95 nm) enables $d \sim 60$. Achieving $d = 128$ requires FSR extension with C+L+S band operation (Supplementary Section S3).

Chip Area Estimation

The 32×256 configuration (8192 MRRs) fits on a single $\sim 5 \times 5$ mm² die; the 64×1024 configuration requires multi-chip packaging or folded layouts. Detailed area estimates are provided in Supplementary Section S4.

Figure 13 summarizes the scaling trend.

Time-Multiplexed Operation

Area and power constraints can be relaxed by trading physical parallelism for temporal reuse via time-multiplexed weight programming [62]. The system deploys N_{phys} physical rows and cycles through M weight configurations:

$$N_{\text{logical}} = M \times N_{\text{phys}}, \quad M = \lceil N/N_{\text{phys}} \rceil. \quad (16)$$

On TFLN, EO reprogramming is sub-nanosecond ($t_{\text{reprogram}} \ll t_{\text{optical}}$), so the total latency simplifies to $t_{\text{total}} \approx M \times t_{\text{optical}}$. Even at $M = 8$, the total latency (80 ns) remains four orders of magnitude below the GPU full-scan baseline (~ 200 μ s)—a fundamental advantage over thermo-optic SOI ($t_{\text{reprogram}} \sim 10$ μ s).

For LLM decode at 128K+ context, $M = 4$ – 8 is a practical sweet spot: it reduces physical MRR count by 4– $8\times$ (to 8192–16 384), keeps chip area within a single reticle, and resolves the area scaling barrier of Sec. , making $d = 64$ realizable with current TFLN technology (fig. 14).

Batch serving with page-by-page evaluation. When the number of cached blocks N exceeds the physical chip capacity N_{chip} , the system pages through $M = \lceil N/N_{\text{chip}} \rceil$ configurations per evaluation. For batch serving with B_{batch} concurrent users, the total selection time per decode step is

$$t_{\text{select}} = B_{\text{batch}} \times H_{\text{KV}} \times L \times M \times (t_{\text{reprogram}} + t_{\text{optical}}), \quad (17)$$

where H_{KV} is the number of KV heads and L the number of layers (time-multiplexed across heads and layers on a single chip). For Qwen2.5-7B ($H_{\text{KV}} = 4$, $L = 28$) with $N_{\text{chip}} = 1024$, $t_{\text{reprogram}} = 4$ ns, and $t_{\text{optical}} = 9$ ns: at 1M context ($M = 8$), batch = 128 yields $t_{\text{select}} = 1.5$ ms; at 10M ($M = 80$), $t_{\text{select}} = 14.9$ ms. Adding model weight reads (4.2 ms) and KV block fetch (8.6 ms), the total per-token decode latency remains $3.5\times$ – $5.3\times$ lower than GPU block selection at 10M–100M context (fig. 16). Unlike GPU full scan, where latency is fundamentally bandwidth-limited at $O(N)$, PRISM paging latency grows as $O(N/N_{\text{chip}})$ with a much smaller constant (13 ns per page vs. ~ 8 ns per block for HBM reads), and can be eliminated entirely by scaling N_{chip} with additional parallel banks.

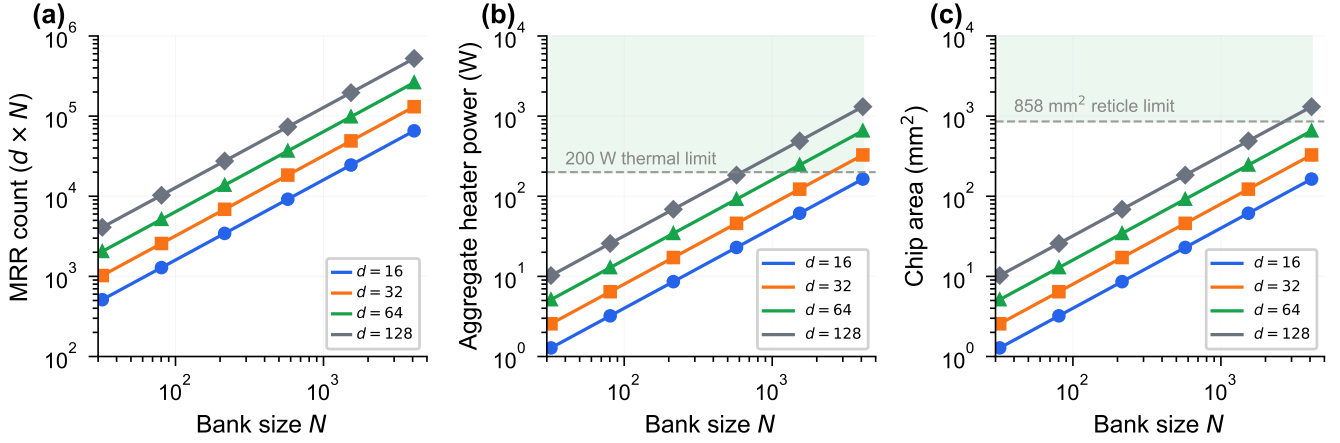


FIG. 13. PRISM photonic scaling projections. MRR count, aggregate heater power (SOI), and estimated chip area as functions of the configuration parameters d and N . The dashed horizontal lines indicate practical limits: 200 W thermal dissipation (active cooling) and 858 mm^2 single-reticle area. Configurations below both limits (shaded region) are realizable on a single photonic chip.

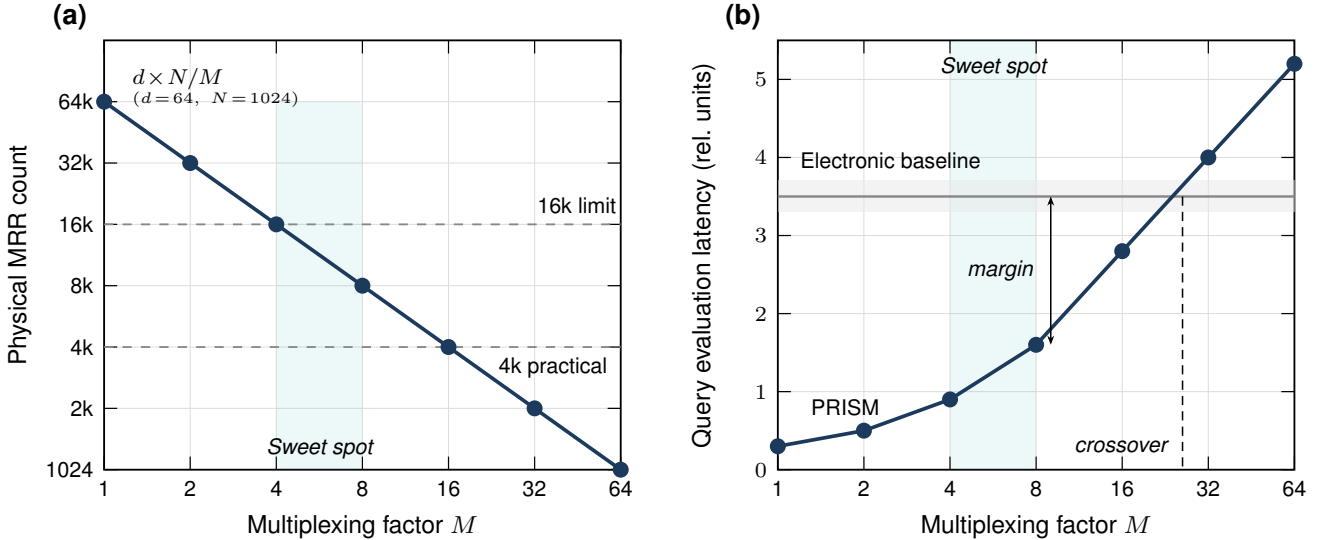


FIG. 14. Time-multiplexed PRISM operation. (a) Physical MRR count vs. multiplexing factor M ($d = 64, N = 1024$). (b) Query evaluation latency vs. M , compared to electronic baselines. The shaded region indicates the sweet spot ($M = 4-8$).

Energy and Latency Crossover

We define the crossover point n^* as the context length at which PRISM-assisted decoding cost equals the electronic baseline. The PRISM cost (photonic selection energy $\sim 2290\text{ pJ}$ per query plus reduced GPU fetch) is compared against the GPU full-scan cost (fetching all N blocks via HBM). On TFLN, near-zero static power means the selection cost is dominated by dynamic components. The full derivation is in Supplementary Section S2.

Energy crossover. Against the GPU full scan (fig. 15a), the mathematical crossover occurs at $n^* < 1\text{K}$ tokens ($d = 64, N_{\text{bank}} = 4$); practical benefit emerges at $n \geq 4\text{K}$ where traffic reduction exceeds $8\times$. The per-query dynamic energy ($\sim 2290\text{ pJ}$; table III) is four orders of magnitude below the H100 fetch energy at 128K context ($\sim 16.3\text{ }\mu\text{J}$). This GPU baseline assumes a full-dimension scan ($d_h=128$). A fairer comparison lets the GPU scan compressed $d=32$ signatures, reducing scan energy to $E_{\text{scan}}^{\text{fair}} \approx 12\text{ }\mu\text{J}$. Even under this fairer comparison where the GPU scans compressed $d=32$ signatures ($\sim 12\text{ }\mu\text{J}$), PRISM maintains a $\sim 5000\times$ advan-

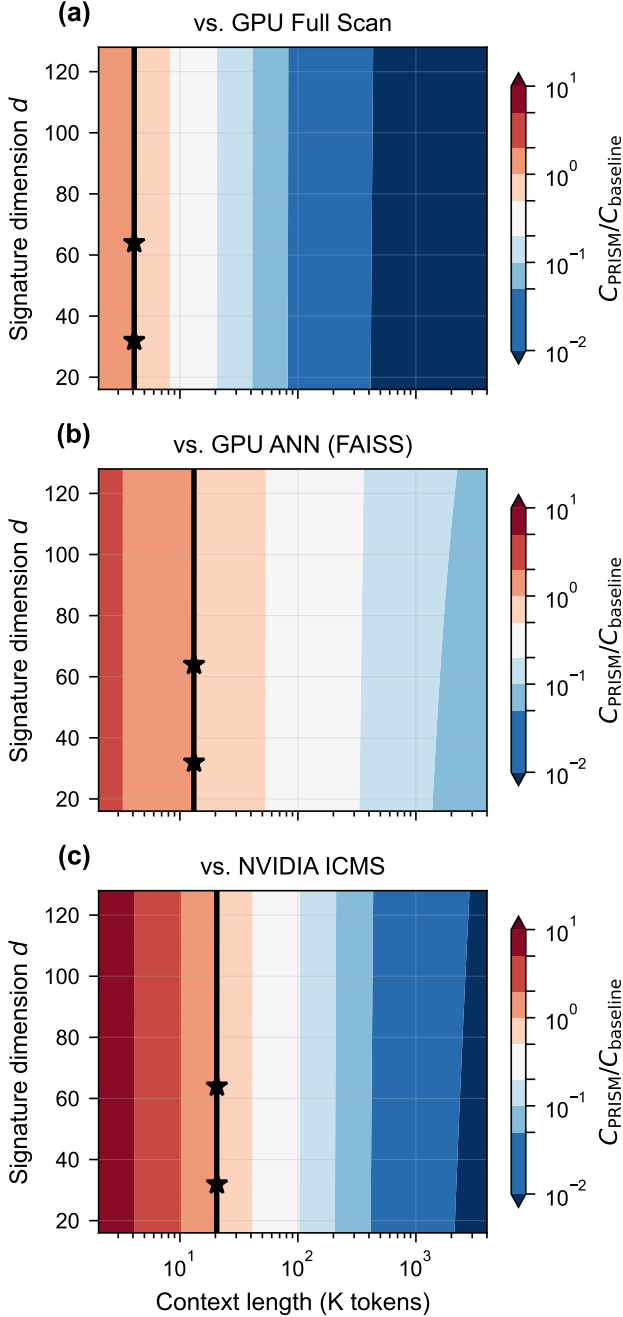


FIG. 15. Energy crossover map for PRISM vs. electronic baselines. The crossover contour ($C_{\text{PRISM}}/C_{\text{baseline}} = 1$) shifts to shorter context lengths as d decreases. (a) vs. GPU full scan: practical benefit at $n^* \approx 4\text{K}$. (b) vs. GPU ANN: $n^* \approx 4\text{K}$. (c) vs. NVIDIA ICMS: $n^* \approx 4\text{K}$.

tage ($\sim 2290\text{ pJ}$ vs. $\sim 12\text{ }\mu\text{J}$), preserving a comfortable crossover margin. On thermo-optic SOI, the $\sim 164\text{ W}$ heater power would place the crossover at $n^* \approx 4\text{K}$. Against GPU ANN (FAISS IVF-PQ) [63] ($O(\sqrt{N})$ scan reduction), the crossover is at $n^* \approx 2\text{K}$. Against NVIDIA ICMS (DPU with lower bandwidth than GPU HBM),

$n^* \approx 4\text{K}$ based on estimated GTC 2024 specifications.

Latency crossover. The $\sim 9\text{ ns}$ photonic evaluation is orders of magnitude below the $\sim 5\text{ }\mu\text{s}$ GPU scan, so the selection step is effectively free in latency terms ($n^* \lesssim 4\text{K}$ tokens).

Sensitivity. The dominant factors are: (i) dynamic power ($\sim 254\text{ mW}$, dominated by TIAs/ADCs, laser, and DACs; table III); (ii) signature dimension d (controls MRR count and area, traded against recall quality, Sec.); (iii) bank count N_{bank} (splitting loss vs. parallelism); and (iv) HBM bandwidth (HBM4 improvements shift the crossover to longer contexts).

Scaling projections. The energy ratio $C_{\text{PRISM}}/C_{\text{GPU}}$ decreases as $\sim 1/n$ because electronic scan cost grows linearly while PRISM selection cost is fixed. At $n = 1\,000\,000$ ($N \approx 8000$ blocks), the GPU reads $\sim 1\text{ MB}$ of signatures per head per query; PRISM accommodates this with $N_{\text{bank}} = 8$ banks (512 000 MRRs total). In multi-agent scenarios, a single weight bank serves A agents simultaneously (only the query sketch changes), amortizing dynamic power by $1/A$.

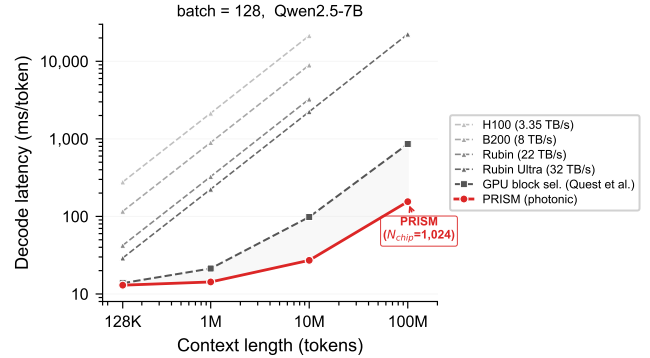


FIG. 16. Per-token decode latency vs. context length for batch serving (batch = 128, Qwen2.5-7B, $B=128$, $k=32$). GPU full-scan latency (dashed gray) is shown for four hardware generations: H100 (3.35 TB/s) [64], B200 (8 TB/s) [65], Vera Rubin (22 TB/s) [8], and Rubin Ultra (32 TB/s HBM4e) [66]. GPU block selection (Quest et al., dark gray) performs $O(N)$ signature scan from HBM. PRISM (red, $N_{\text{chip}} = 1024$) uses page-by-page time-multiplexing (eq. (17)) when $N > N_{\text{chip}}$, growing as $O(N/N_{\text{chip}})$ but with a per-page cost of only 13 ns. Latency is computed as $t = t_{\text{weights}} + t_{\text{select}} + t_{\text{fetch}}$, where $t_{\text{weights}} = 14\text{ GB}/\text{BW}_{\text{HBM}}$ and $t_{\text{fetch}} = \text{batch} \times kB \times 2d_h b_{\text{prec}} \times H_{\text{KVL}}/\text{BW}_{\text{HBM}}$.

DISCUSSION

Limitations and Practical Considerations

All hardware results in this work are based on device-level simulations with parameters extracted from FDTD and supplemented by literature values; no physical pro-

prototype has been fabricated or measured. The impairment models, while grounded in FDTD simulation and published device data, may not capture all fabrication-dependent effects such as waveguide roughness variations, EO electrode non-uniformity across a large array, and packaging-induced stress. At $d = 64$ and $N = 1024$, the system requires 65 536 MRRs; systematic characterization of $>10\,000$ -MRR arrays on TFLN has not been reported, though recent progress in TFLN foundry processes suggests that large-scale integration is feasible [45]. Fabrication non-uniformity causes resonance wavelength variations of $\sigma_\lambda \sim 0.5$ nm to 2 nm across a wafer [17], but on the TFLN platform EO tuning can compensate via DC bias adjustment without static power penalty. Residual thermal drift, while mitigated by lithium niobate’s $\sim 4\times$ lower thermo-optic coefficient compared to silicon, still requires chip-level thermal stabilization (~ 1 W TEC budget). The 1 W TEC is a fixed overhead independent of query rate; at a throughput of T head-queries per second the amortized TEC contribution is $1/T$ joules per head-query. For $T = 10^5$ (e.g., 100 concurrent users \times 1000 tokens/s), TEC adds ~ 10 μ J per head-query, bringing the total to ~ 12.3 μ J. The 2290 pJ value cited elsewhere in this paper refers to the dynamic photonic pipeline alone.

Interface latency. The ~ 9 ns latency reported for PRISM reflects the photonic pipeline alone (DAC through top- k selection) and does not include the host interface overhead. A PCIe 5.0 round-trip (DMA setup and transfer) adds ~ 1 μ s to 2 μ s; CXL-attached memory semantics reduce this to ~ 200 ns to 500 ns; direct interposer or co-packaged integration would add only ~ 10 ns to 50 ns. Even with PCIe overhead, the total system latency of ~ 2 μ s remains below the GPU full-scan latency (~ 5 μ s), yielding a system-level 2–3 \times speedup. Co-packaging—the long-term integration target—would preserve the $\sim 100\times$ raw photonic advantage. Speedup claims should therefore be interpreted as system-level 2–3 \times with PCIe, potentially 100 \times with co-packaging.

Demonstrated vs. projected scale. To clarify the maturity of the MRR integration scales assumed in this work: demonstrated TFLN arrays have reached ~ 10 –100 MRRs [45], while SOI platforms have demonstrated ~ 1000 –10 000 MRRs [35]. PRISM’s “current” configuration (8192 MRRs at $d=32$, $N=256$) is a *projected* design point that extrapolates from these demonstrations; the flagship configuration (65 536 MRRs at $d=64$, $N=1024$) is also projected and would likely require multi-chip or wafer-scale integration.

At $d = 64$ and $N = 1024$, the system requires 65 536 individually addressable voltage bias lines for fabrication-offset compensation of each MRR, presenting a significant packaging and routing challenge that will require advanced fan-out or interposer-based solutions.

The add-drop MRR configuration with balanced photodetection resolves the sign limitation of through-port-

only architectures. The balanced differential photocurrent $I_{\text{through}} - I_{\text{drop}}$ naturally encodes signed weights in $[-1, +1]$, enabling true signed inner products without ReLU projection or split encoding. The trade-off is a doubling of the photodetector count (two PDs per channel), but since PDs are orders of magnitude smaller than MRRs, the area penalty is negligible.

The retrieval head classification threshold $\tau = 0.3$ used throughout this work becomes less discriminative at longer contexts, where most heads tend to exhibit high retrieval scores; DuoAttention’s learned gating identifies only 25–50% of heads as retrieval heads. The 90%+ fraction reported here should therefore be interpreted as an upper bound estimate at the evaluated context lengths.

For multi-head serving, GQA [29] reduces the number of independent weight bank instances from the retrieval head count (102 for Qwen2.5-7B) to the KV head count ($H_{\text{KV}} = 4$), since block signatures are derived from key vectors at KV-head granularity. This synergy deepens as the field trends toward more aggressive key-value sharing: under multi-query attention ($H_{\text{KV}} = 1$), a single weight bank per layer would suffice. These 4 heads can be served by time-multiplexed reprogramming (~ 4 ns on TFLN, negligible vs. the ~ 5 μ s KV fetch) or by parallel replication of 4 weight banks. When the layer dimension is included, the full configuration space is $H_{\text{KV}} \times L = 4 \times 28 = 112$ weight bank instances per decode step. Under time-multiplexing, this amounts to $112 \times \sim 1$ ns ≈ 112 ns total reprogramming overhead—still $\sim 45\times$ smaller than a single KV block fetch (~ 5 μ s) and therefore negligible in the decode-step budget. Alternatively, a layer-parallel deployment with 28 PRISM chips (one per layer, each serving 4 KV heads) would eliminate the layer serialization entirely at the cost of additional chip area.

Comparison with Related Approaches

The block-level top- k selection mechanism at the core of PRISM builds on a strategy independently validated by several works: Quest [14] preserves over 99% of full-attention accuracy on long-context benchmarks including NIAH up to 1M tokens, DuoAttention [19] maintains LongBench performance within 1–2% of full attention, and InfLLM [21] and RocketKV [15] provide additional evidence for block-level selection at long context. PRISM’s contribution is orthogonal: the key question is not whether block selection preserves quality (answered affirmatively above) but whether MRR-based analog computation introduces sufficient error to degrade the selection. Our NIAH results (Sec.) confirm that it does not, even under pessimistic hardware impairments.

Tian et al.’s photonic transformer chip (PTC) [12] demonstrates that coherent optical interference can implement full transformer attention with high throughput

(>200 POPS); however, it targets dense attention computation rather than the coarse block-selection task addressed by PRISM, and its $O(n)$ memory access scaling remains for long-context KV caches.

InfLLM is the most directly comparable system, as it offloads the full KV cache to CPU RAM and retrieves blocks via electronic inner products. The key distinction is selection latency scaling: InfLLM’s selection time grows as $O(N)$ with the number of cached blocks, while PRISM’s photonic engine evaluates all N similarities in $O(1)$ optical transit time. This advantage grows with context length—precisely the regime where the KV cache bottleneck is most severe.

Relative to Quest [14] and RocketKV [15], which perform block selection *digitally* on the GPU, PRISM targets a different bottleneck: these methods reduce *compute* by pruning low-scoring KV blocks but still require the GPU to read all block signatures from HBM (costing $O(N)$ memory traffic per decode step). In short, RocketKV reduces the number of fetched KV blocks, but still requires scanning all candidates; PRISM eliminates the scan itself. The key enabler is that PRISM stores block signatures directly in the MRR weight bank (programmed incrementally as each block completes, every B tokens), so no HBM read is needed at decode time—whereas Quest and RocketKV must read all N signatures from HBM at *every* decode step. Quest- or RocketKV-style scoring policies could be used to *define* which blocks are selected, while PRISM accelerates the *execution* of that selection. Table VIII quantifies how the scan fraction of total HBM traffic grows with context length, showing that the signature scan—which PRISM eliminates—becomes the dominant cost at long contexts.

TABLE VIII. Signature scan as a fraction of total decode-step HBM traffic (electronic block selection, $d=32$, $k=32$, $B=128$, $d_h=128$). At million-token contexts the scan dominates; PRISM removes this cost entirely.

Context	N (blocks)	Scan / step	Scan fraction
16K	128	8 KB	0.4%
128K	1,024	64 KB	3%
1M	8,192	512 KB	20%
10M	81,920	5 MB	71%
100M	819,200	50 MB	95%

Electronic ASIC alternative. An electronic ASIC could, in principle, also implement parallel selection through massive parallelism. However, such an approach requires N -way replicated compute units, local storage for all N signatures, and high-fan-out interconnect, leading to scaling challenges in area, power, and routing complexity as N grows. In contrast, PRISM leverages the natural broadcast property of photonic systems, where a single query can be passively distributed to all candidates without explicit data movement, making scan-

free selection physically native to the hardware rather than architecturally forced. The key contribution of this work is not limited to a specific photonic implementation, but rather the identification of selection as a memory-read bottleneck and the demonstration that removing the $O(N)$ scan fundamentally changes system scaling. PRISM should be viewed as a hardware instantiation of scan-free selection, particularly natural in photonic broadcast systems.

Table IX summarizes the fundamental distinction between these approaches.

TABLE IX. Comparison of KV cache block-selection strategies ($N = 1024$ blocks, $d = 32$, $k = 32$, H100 GPU baseline). GPU values estimated from H100 datasheet (3.35 TB/s HBM3, 0.71 pJ/MAC); PRISM values from device-physics simulation.

	GPU–HBM full scan	GPU block selection	Prism selective fetch
Scan eliminated?	No	No	Yes
Selection latency	$\sim 5 \mu\text{s}$	$\sim 1\text{--}5 \mu\text{s}$	$\sim 9 \text{ ns}$
Selection energy	$\sim 16.3 \mu\text{J}$	$\sim 4\text{--}16 \mu\text{J}$	$\sim 2.3 \text{ nJ}$
HBM traffic	100%	$\sim 3\% + \text{scan}$	$\sim 3\% \text{ only}$
Scales with N	$O(N)$	$O(N)$	$O(1)$

The GPU ANN baseline used in our crossover analysis (FAISS IVF-PQ [63]) represents a well-established but not state-of-the-art GPU search library; more recent GPU-accelerated ANN libraries (e.g., CAGRA, cuVS) may further reduce the electronic baseline latency and energy, narrowing the crossover window.

NVIDIA’s ICMS [9] addresses the complementary *capacity* problem (terabyte-scale flash-backed KV storage with DPU-managed prefetch), while PRISM solves the *selection* problem via photonic parallel inner products. Note that the ICMS energy and bandwidth specifications used in our comparisons are estimated from public announcements; no published measurements are available, and actual performance may differ. A natural integration would place PRISM within or adjacent to the ICMS, combining storage capacity with photonic selection speed. The recently announced NVIDIA Rubin platform [67] further underscores industry momentum toward dedicated KV cache acceleration hardware, complementary to PRISM’s photonic approach.

Complementary compression. KVTC [68] applies transform coding (PCA decorrelation, adaptive quantization, and entropy coding) to compress KV caches by $\sim 20\times$ with negligible accuracy loss (ICLR 2026). KVTC and PRISM are orthogonal: KVTC reduces the *size* of each stored block (capacity problem), while PRISM eliminates the $O(N)$ signature scan for block selection (access pattern problem). Combining both would yield simultaneous $20\times$ storage reduction and $O(1)$ selection. Note that KVTC’s PCA-transformed representations may require adapting the block signature computation to the

decorrelated basis, which we leave for future work.

Outlook

The immediate next step is fabrication of a small-scale TFLN MRR prototype (8×8 weight bank) to validate inner-product accuracy under real device impairments and provide measured values for parameters currently extracted from simulation. Scaling to a full module ($d = 64$, $N = 256$) integrated with GPU-based LLM inference would validate the crossover predictions of Sec. . Integrating non-volatile weight storage (e.g., phase-change trimming [69, 70]) could further reduce switching energy for quasi-static block signatures [37, 71]. More challenging benchmarks such as SCBench [72] and query-focused retrieval analysis [73] would strengthen confidence in the robustness of photonically selected blocks beyond the NIAH validation presented here.

Practical integration. A deployable PRISM module would package the photonic chip, laser source, and TEC onto a single substrate, offered in one of three form factors: a PCIe add-in card for drop-in datacenter use, a CXL-attached device for lower-latency memory-semantic access, or a co-packaged chiplet on an interposer for maximum performance. Integration with existing LLM serving stacks (e.g., vLLM, TensorRT-LLM) would proceed via a block-index API: the host submits a query sketch and receives ranked block indices, transparently replacing the software signature-scan kernel.

Benchmark scope. NIAH is a retrieval-oriented benchmark that tests single-needle recall; it does not exercise multi-hop reasoning, summarization, or other long-context capabilities. To assess generalization beyond NIAH, we evaluated PRISM block selection on three LongBench-v2 domains (table X). Across all domains, MRR-impaired block selection (5-bit, 20 pm drift) produces *identical* accuracy to full attention, confirming that the block-selection approximation introduces no measurable quality loss on diverse long-context tasks.

TABLE X. LongBench-v2 accuracy (%) with PRISM block selection (Qwen2.5-7B, $k=32$, $B=128$, $d=32$, 4K context, 5-bit quantization, 20 pm drift).

Domain	Full attn.	PRISM	Drop
Multi-Document QA	16.7	16.7	0.0
Single-Document QA	23.3	23.3	0.0
Long In-context Learning	26.7	26.7	0.0
Overall	22.2	22.2	0.0

We note that the block selection mechanism is inherited from Quest [14] and InfLLM [21], which have been validated on broader benchmarks (LongBench, ∞ Bench); PRISM’s contribution is the photonic hardware mapping of this selection, not the selection algorithm itself.

CONCLUSION

We have presented PRISM, a TFLN photonic similarity engine that computes all N block-selection inner products in $O(1)$ optical latency via the broadcast-and-weight paradigm. End-to-end NIAH evaluation confirms that MRR-selected block-sparse attention preserves full-attention accuracy from 4K to 64K tokens (within the model’s native context window) under realistic hardware impairments (4–5 bit weights, 30 pm thermal drift), while reducing KV cache traffic by $16\times$ at 64K context ($k=32$, $B=128$; $32\times$ at 128K). At longer contexts (128K+), model-intrinsic accuracy degrades independent of block selection; the photonic scaling analysis nevertheless projects favorable energy and latency scaling to million-token regimes as model context windows continue to expand. The practical energy benefit emerges at $n \geq 4K$ where block selection yields meaningful traffic reduction, making PRISM favorable across virtually all practical context lengths.

Future work will proceed along three axes: (i) fabrication and characterization of an 8×8 TFLN MRR weight bank to validate simulation predictions with measured device parameters; (ii) scaling to a full $d=64$, $N=256$ module integrated with GPU-based inference for end-to-end latency and energy measurements; and (iii) integration of non-volatile weight storage (e.g., phase-change trimming [69, 70]) for write-once signature programming, together with hardware-aware learned projections and broader benchmarks such as SCBench [72]. More broadly, photonic broadcast search may serve as a general paradigm for similarity-search workloads in data centers—including approximate nearest-neighbor retrieval, recommendation ranking, and embedding lookup—wherever a single query must be compared against a large, slowly changing set of stored vectors.

DISCLOSURES

The authors declare no conflicts of interest.

DATA AVAILABILITY

Code and simulation data are available at <https://github.com/hyoseokp/PRISM> [74].

* Corresponding author: yeonsang.park@cnu.ac.kr

- [1] T. Dao, in *International Conference on Learning Representations* (2024) arXiv:2307.08691 (2023).
- [2] A. Gholami, Z. Yao, S. Kim, C. Hooper, M. W. Mahoney, and K. Keutzer, *IEEE Micro* **44**, 33 (2024).

- [3] OpenAI, Introducing GPT-5.4, <https://openai.com/index/introducing-gpt-5-4/> (2026), 1M token context window, native computer use. Released March 5, 2026.
- [4] Anthropic, 1m context is now generally available for Opus 4.6 and Sonnet 4.6, <https://claude.com/blog/1m-context-ga> (2026), 1M token context window at standard pricing. March 13, 2026.
- [5] Gemini Team Google, arXiv preprint arXiv:2403.05530 (2024).
- [6] Meta AI, The Llama 4 herd: The beginning of a new era of natively multimodal AI innovation, <https://ai.meta.com/blog/llama-4-multimodal-intelligence/> (2026), llama 4 Scout: 17B active params, 10M token context window.
- [7] Qwen Team, arXiv preprint arXiv:2501.15383 (2025).
- [8] NVIDIA, NVIDIA Vera Rubin Platform, <https://nvidianews.nvidia.com/news/nvidia-vera-rubin-platform> (2026), announced at GTC 2026; next-generation AI platform with Rubin GPU, Vera CPU, HBM4, and integrated memory connectivity.
- [9] NVIDIA, Inference Context Memory Storage (ICMS): BlueField-4 DPU for LLM Inference, <https://nvidianews.nvidia.com/news/nvidia-bluefield-4-powers-new-class-of-ai-native-storage> (2026), flash-backed KV cache with hardware-assisted eviction and prefetch. Announced CES 2026.
- [10] S. Hua, E. Divita, S. Yu, B. Peng, C. Roques-Carmes, Z. Su, Z. Chen, Y. Bai, J. Zou, Y. Zhu, Y. Xu, C. Lu, Y. Di, H. Chen, L. Jiang, L. Wang, L. Ou, C. Zhang, J. Chen, W. Zhang, H. Zhu, W. Kuang, L. Wang, H. Meng, M. Steinman, and Y. Shen, *Nature* **640**, 361 (2025).
- [11] H. Zhu, J. Gu, H. Wang, Z. Jiang, Z. Zhang, R. Tang, C. Feng, S. Han, R. T. Chen, and D. Z. Pan, in *Proc. IEEE International Symposium on High-Performance Computer Architecture (HPCA)* (2024) pp. 686–703.
- [12] Y. Tian, S. Xiang, X. Guo, Y. Zhang, J. Xu, S. Shi, H. Zhao, Y. Wang, X. Niu, W. Liu, and Y. Hao, *Photonix* **6**, 45 (2025).
- [13] T. Fu, J. Zhang, R. Sun, Y. Huang, W. Xu, S. Yang, Z. Zhu, and H. Chen, *Light: Science & Applications* **13**, 10.1038/s41377-024-01590-3 (2024).
- [14] J. Tang, Y. Zhao, K. Zhu, G. Xiao, B. Kasikci, and S. Han, arXiv preprint arXiv:2406.10774 (2024).
- [15] P. Behnam, Y. Fu, R. Zhao, P.-A. Tsai, Z. Yu, and A. Tumanov, in *International Conference on Machine Learning (ICML)* (2025).
- [16] A. N. Tait, M. A. Nahmias, B. J. Shastri, T. F. de Lima, and P. R. Prucnal, *Journal of Lightwave Technology* **32**, 3427 (2014).
- [17] A. N. Tait, T. F. de Lima, M. A. Nahmias, B. J. Shastri, and P. R. Prucnal, *IEEE Journal of Selected Topics in Quantum Electronics* **22**, 5900110 (2016).
- [18] W. Wu, Y. Wang, G. Xiao, H. Peng, and Y. Fu, in *International Conference on Learning Representations (ICLR)* (2025) oral presentation.
- [19] G. Xiao, J. Tang, J. Zuo, J. Guo, S. Yang, H. Tang, Y. Fu, and S. Han, in *International Conference on Learning Representations (ICLR)* (2025).
- [20] H. Tang, Y. Lin, J. Lin, Q. Han, S. Hong, Y. Yao, and G. Wang, arXiv preprint arXiv:2407.15891 (2024).
- [21] C. Xiao, P. Zhang, X. Han, G. Xiao, Y. Lin, Z. Zhang, Z. Liu, S. Han, and M. Sun, arXiv preprint arXiv:2402.04617 (2024).
- [22] X. Liu, Z. Tang, P. Dong, Z. Li, B. Li, X. Hu, and X. Chu, in *Advances in Neural Information Processing Systems (NeurIPS)* (2025).
- [23] H. Li, Y. Li, A. Tian, T. Tang, Z. Xu, X. Chen, N. Hu, W. Dong, Q. Li, and L. Chen, *Transactions on Machine Learning Research* (2025).
- [24] Z. Zhang, Y. Sheng, T. Zhou, T. Chen, L. Zheng, R. Cai, Z. Song, Y. Tian, C. Ré, C. Barrett, Z. Wang, and B. Chen, in *Advances in Neural Information Processing Systems (NeurIPS)* (2023).
- [25] G. Xiao, Y. Tian, B. Chen, S. Han, and M. Lewis, in *International Conference on Learning Representations (ICLR)* (2024) arXiv:2309.17453.
- [26] C. Hooper, S. Kim, H. Mohammadzadeh, M. W. Mahoney, Y. S. Shao, K. Keutzer, and A. Gholami, in *Advances in Neural Information Processing Systems (NeurIPS)* (2024).
- [27] G. Liu, C. Li, Z. Ning, J. Lin, Y. Yao, D. Ke, M. Guo, and J. Zhao, arXiv preprint arXiv:2505.13109 (2025).
- [28] A. Vaswani, N. Shazeer, N. Parmar, J. Uszkoreit, L. Jones, A. N. Gomez, L. Kaiser, and I. Polosukhin, in *Advances in Neural Information Processing Systems*, Vol. 30 (2017) pp. 5998–6008.
- [29] J. Ainslie, J. Lee-Thorp, M. de Jong, Y. Zemlyanskiy, E. Levent and Sr Saigra, in *Proceedings of the 2023 Conference on Empirical Methods in Natural Language Processing (EMNLP)* (2023) pp. 4895–4901.
- [30] N. Shazeer, arXiv preprint arXiv:1911.02150 (2019).
- [31] M. Reck, A. Zeilinger, H. J. Bernstein, and P. Bertani, *Physical Review Letters* **73**, 58 (1994).
- [32] W. R. Clements, P. C. Humphreys, B. J. Metcalf, W. S. Kolthammer, and I. A. Walmsley, *Optica* **3**, 1460 (2016).
- [33] Y. Shen, N. C. Harris, S. Skirlo, M. Prabhu, T. Baehr-Jones, M. Hochberg, X. Sun, S. Zhao, H. Larochelle, D. Englund, and M. Soljačić, *Nature Photonics* **11**, 441 (2017).
- [34] H. Zhou, J. Dong, J. Cheng, W. Dong, C. Huang, Y. Shen, Q. Zhang, M. Gu, C. Qian, H. Chen, Z. Ruan, and X. Zhang, *Light: Science & Applications* **11**, 30 (2022).
- [35] C. Huang, S. Bilodeau, T. F. de Lima, A. N. Tait, P. Y. Ma, E. C. Blow, A. Jha, H.-T. Peng, B. J. Shastri, and P. R. Prucnal, *APL Photonics* **5**, 040803 (2020).
- [36] Q. Xu, B. Schmidt, S. Pradhan, and M. Lipson, *Nature* **435**, 325 (2005).
- [37] H. Zhang, Y. Song, S. Chen, Y. Bai, X. Xu, C. Huang, J. Wang, H. Chen, D. J. Moss, and K. Xu, *npj Nanophotonics* **2**, 40 (2025).
- [38] W. B. Johnson and J. Lindenstrauss, *Contemporary Mathematics* **26**, 189 (1984).
- [39] C. Wang, M. Zhang, X. Chen, M. Bertrand, A. Shams-Ansari, S. Chandrasekhar, P. Winzer, and M. Lončar, *Nature* **562**, 101 (2018).
- [40] B. J. Shastri, A. N. Tait, T. Ferreira de Lima, W. H. P. Pernice, H. Bhaskaran, C. D. Wright, and P. R. Prucnal, *Nature Photonics* **15**, 102 (2021).
- [41] A. Totovic, G. Giamougiannis, A. Tsakyridis, D. Lazovsky, and N. Pleros, *Scientific Reports* **12**, 5605 (2022).
- [42] S. Lischke, A. Peczek, J. S. Morgan, K. Sun, D. Steckler, Y. Yamamoto, F. Korndörfer, C. Mai, S. Marschmeyer, M. Fraschke, A. Krüger, A. Beling, and L. Zimmermann, *Nature Photonics* **15**, 925 (2021).
- [43] N. Peserico, B. J. Shastri, and V. J. Sorger, *Journal of Lightwave Technology* **41**, 3704 (2023).

- [44] J. Feldmann, N. Youngblood, M. Karpov, H. Gehring, X. Li, M. Stappers, M. Le Gallo, X. Fu, A. Lukashchuk, A. S. Raja, J. Liu, C. D. Wright, A. Sebastian, T. J. Kippenberg, W. H. P. Pernice, and H. Bhaskaran, *Nature* **589**, 52 (2021).
- [45] Y. Hu, Y. Song, X. Zhu, X. Guo, S. Lu, Q. Zhang, L. He, C. A. A. Franken, K. Powell, H. Warner, *et al.*, *Nature Communications* **16**, 8178 (2025).
- [46] X. Zhu, Y. Hu, S. Lu, H. K. Warner, X. Li, Y. Song, L. S. Magalhães, A. Shams-Ansari, N. Sinclair, and M. Lončar, *Photonics Research* **12**, A7 (2024).
- [47] A. N. Tait, T. F. de Lima, E. Zhou, A. X. Wu, M. A. Nahmias, B. J. Shastri, and P. R. Prucnal, *Scientific Reports* **7**, 7430 (2017).
- [48] H. Park and Y. Park, arXiv preprint arXiv:2603.12934 (2026).
- [49] W. Bogaerts, P. De Heyn, T. Van Vaerenbergh, K. De Vos, S. Kumar Selvaraja, T. Claes, P. Dumon, P. Bienstman, D. Van Thourhout, and R. Baets, *Laser & Photonics Reviews* **6**, 47 (2012).
- [50] T. Ferreira de Lima, E. A. Doris, S. Bilodeau, W. Zhang, A. Jha, H.-T. Peng, E. C. Blow, C. Huang, A. N. Tait, B. J. Shastri, and P. R. Prucnal, *Nanophotonics* **11**, 3805 (2022).
- [51] K. Padmaraju and K. Bergman, *Nanophotonics* **3**, 269 (2014).
- [52] F. Sunny, A. Mirza, M. Nikdast, and S. Pasricha, in *Proc. 58th ACM/IEEE Design Automation Conference (DAC)* (2021) pp. 1069–1074.
- [53] J. Choquette, *IEEE Micro* **43**, 9 (2023).
- [54] Qwen Team, arXiv preprint arXiv:2412.15115 (2024).
- [55] Qwen Team, arXiv preprint arXiv:2505.09388 (2025).
- [56] P. Indyk and R. Motwani, in *Proceedings of the 30th Annual ACM Symposium on Theory of Computing (STOC)* (1998) pp. 604–613.
- [57] C. D. Manning, P. Raghavan, and H. Schütze, *Introduction to Information Retrieval* (Cambridge University Press, 2008).
- [58] G. Kamradt, Needle in a haystack — pressure testing LLMs, https://github.com/gkamradt/LLMTest_NeedleInAHaystack (2023).
- [59] S. Shekhar, W. Bogaerts, L. Chrostowski, J. E. Bowers, M. Hochberg, R. Soref, and B. J. Shastri, *Nature Communications* **15**, 751 (2024).
- [60] T. J. Seok, K. Kwon, J. Henriksson, J. Luo, and M. C. Wu, *Optica* **6**, 490 (2019).
- [61] P. Dong, *IEEE Journal of Selected Topics in Quantum Electronics* **22**, 370 (2016).
- [62] Y. Bai, X. Xu, M. Tan, Y. Sun, Y. Li, J. Wu, R. Morandotti, A. Mitchell, K. Xu, and D. J. Moss, *Nanophotonics* **12**, 795 (2023).
- [63] J. Johnson, M. Douze, and H. Jégou, *IEEE Transactions on Big Data* **7**, 535 (2021).
- [64] NVIDIA, NVIDIA H100 Tensor Core GPU Datasheet, <https://www.nvidia.com/en-us/data-center/h100/> (2023), 80 GB HBM3, 3.35 TB/s memory bandwidth.
- [65] NVIDIA, NVIDIA Blackwell B200 GPU, <https://www.nvidia.com/en-us/data-center/dgx-b200/> (2025), 192 GB HBM3e, 8 TB/s memory bandwidth.
- [66] NVIDIA, NVIDIA Rubin Ultra GPU with HBM4e, <https://videocardz.com/newz/nvidia-unveils-rubin-ultra-with-1tb-hbm4e-memory-for-2027-feynman-architecture-in-2028> (2027), 1 TB HBM4e, ~32 TB/s bandwidth; announced at GTC 2025.
- [67] K. Aubrey, [Inside the NVIDIA Vera Rubin platform: Six new chips, one AI supercomputer](#), NVIDIA Developer Blog (2026).
- [68] K. Staniszewski and A. Łańcucki, in *International Conference on Learning Representations (ICLR)* (2026) arXiv:2511.01815.
- [69] B. Tossoun, D. Liang, S. Cheung, Z. Fang, X. Sheng, J. P. Strachan, and R. G. Beausoleil, *Nature Communications* **15**, 551 (2024).
- [70] U. Adya, S. Singhal, R. Chen, I.-T. Chen, S. Joshi, A. Majumdar, M. Li, and S. Moazeni, *Nature Communications* **16**, 9290 (2025).
- [71] F. Fayza, C. Demirkiran, S. P. Rao, D. Bunandar, U. Gupta, and A. Joshi, *Communications Physics* **8**, 10.1038/s42005-025-02300-0 (2025).
- [72] Y. Li, H. Jiang, Q. Wu, X. Luo, S. Ahn, C. Zhang, A. H. Abdi, D. Li, J. Gao, Y. Yang, and L. Qiu, in *International Conference on Learning Representations (ICLR)* (2025).
- [73] W. Zhang, F. Yin, H. Yen, D. Chen, and X. Ye, arXiv preprint arXiv:2506.09944 (2025).
- [74] H. Park and Y. Park, PRISM: Photonic retrieval-index similarity module — experiment code, <https://github.com/hyoseokp/PRISM> (2025), source code for retrieval-head identification, signature generation, recall measurement, hardware-aware simulation, and downstream evaluation.

SUPPLEMENTARY INFORMATION

Device Impairment Models

This section provides the full mathematical models for the six impairment sources that degrade the ideal inner-product computation of eq. (6).

Weight quantization. MRR transmission is programmed via electro-optic tuning with finite precision. We model the quantized weight as

$$\hat{w}_{n,j} = \frac{\text{round}(w_{n,j} \cdot 2^b)}{2^b}, \quad (\text{S1})$$

where b is the effective bit precision. Values of $b = 4$ – 8 are considered, corresponding to 16–256 distinguishable transmission levels.

Thermal drift. After initial calibration, the MRR resonance wavelength drifts due to ambient temperature fluctuations. We model the drift as a Gaussian random walk:

$$\Delta\lambda_0(t) = \sum_{i=1}^{t/\Delta t} \mathcal{N}(0, \sigma_{\text{drift}}^2), \quad (\text{S2})$$

with σ_{drift} chosen to produce a standard deviation of 0.01 nm to 0.1 nm over a calibration interval T_{cal} . The resulting weight error is

$$\Delta w = \left| \frac{\partial T}{\partial \lambda} \right| \Delta\lambda_0 \approx \frac{8Q^2 D_{\text{max}}}{\lambda_0^2} \cdot \Delta\lambda_0, \quad (\text{S3})$$

evaluated at the operating point on the MRR Lorentzian. Note that the i.i.d. Gaussian model above does not capture spatially correlated drift (e.g., center-to-edge temperature gradients across the chip), which could cause systematic bias in the inner-product scores rather than zero-mean random noise; such gradients would require a correlated noise model or per-region calibration.

Insertion loss. Each MRR introduces an off-resonance insertion loss $\text{IL}_{\text{MRR}} \approx 0.02$ dB to 0.05 dB, and the $1 \times N$ splitter contributes IL_{split} from eq. (8). The total channel loss is

$$\text{IL}_{\text{total}} = \text{IL}_{\text{split}} + d \cdot \text{IL}_{\text{MRR}} + \text{IL}_{\text{wg}}, \quad (\text{S4})$$

where IL_{wg} accounts for waveguide propagation loss (~ 0.3 dB/cm for TFLN). High insertion loss reduces the SNR at the photodetector and increases the required laser power.

Photodetector noise. The photocurrent at each detector includes shot noise and thermal noise:

$$\sigma_I^2 = 2eI_{\text{ph}} \Delta f + \frac{4k_B T}{R_L} \Delta f + \text{NEP}^2 \cdot \Delta f, \quad (\text{S5})$$

where I_{ph} is the signal photocurrent, Δf is the detection bandwidth, R_L is the load resistance, and NEP is the noise-equivalent power of the photodetector (~ 10 pW/ $\sqrt{\text{Hz}}$ for Ge-on-Si) [1, 2]. The noise introduces a random perturbation to the inner-product score, potentially reordering the top- k ranking.

MRR crosstalk. Adjacent MRRs on the same bus waveguide can exhibit spectral overlap if the channel spacing is insufficient relative to the MRR linewidth. We model inter-channel crosstalk as an additive interference with isolation of -15 dB to -30 dB:

$$y_n = \sum_{j=1}^d w_{n,j} s_j + \sum_{j=1}^d \sum_{m \neq j} \chi_{j,m} w_{n,m} s_m, \quad (\text{S6})$$

where $\chi_{j,m}$ is the crosstalk coefficient from channel m to channel j [3].

Input DAC noise. The finite resolution and integral nonlinearity (INL) of the input DACs contribute an additional noise floor on the query sketch values. At $b_{\text{DAC}} = 6$ bits, the quantization noise standard deviation is $\sigma_{\text{DAC}} = 2^{-b_{\text{DAC}}} / \sqrt{12} \approx 0.0045$.

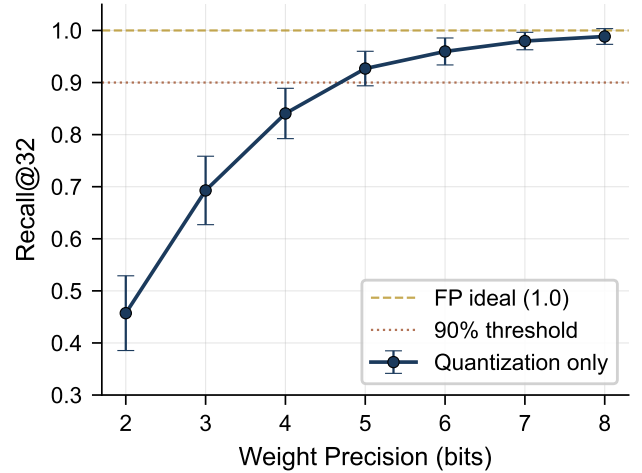


FIG. S1. Impact of weight quantization on recall. At $b = 6$ bits, recall degrades by less than 5% from the floating-point ideal ($\text{Recall}@8 = 0.960$ at 6-bit). Adding thermal drift ($\sigma_{\text{th}} = 0.01$) and detector noise ($\sigma_{\text{det}} = 0.01$) degrades recall by an additional 5%.

Optical Link Budget Details

Latency Breakdown

The PRISM latency is the sum of the five pipeline stages:

$$t_{\text{PRISM}} = t_{\text{DAC}} + t_{\text{opt}} + t_{\text{PD}} + t_{\text{ADC}} + t_{\text{top-}k}, \quad (\text{S7})$$

where the optical propagation time t_{opt} includes the modulator response, waveguide transit, and MRR ring-down time.

TABLE S1. Optical link budget for $d = 32$, $N = 256$ ($P_{\text{laser}} = 20$ dBm).

Element	Loss (dB)	Cumulative (dBm)
Laser output	—	+20.0
Fiber-chip coupling	-2.0	+18.0
MZM modulator (avg.)	-3.0	+15.0
1×256 splitter	-25.7 ^a	-10.7
Waveguide (2 cm)	-1.0	-11.7
$d=32$ MRR (balanced, worst-case drop)	-3.2 ^b	-14.9
Chip-detector coupling	-1.0	-15.9
Per-PD optical power		-15.9 dBm

^a $10 \log_{10}(256) + 0.2 \times 8 = 24.1 + 1.6 = 25.7$ dB. ^b Drop-port 0.1 dB + 31×0.05 dB through-port = 1.65 dB; rounded to 3.2 dB with alignment margin [4].

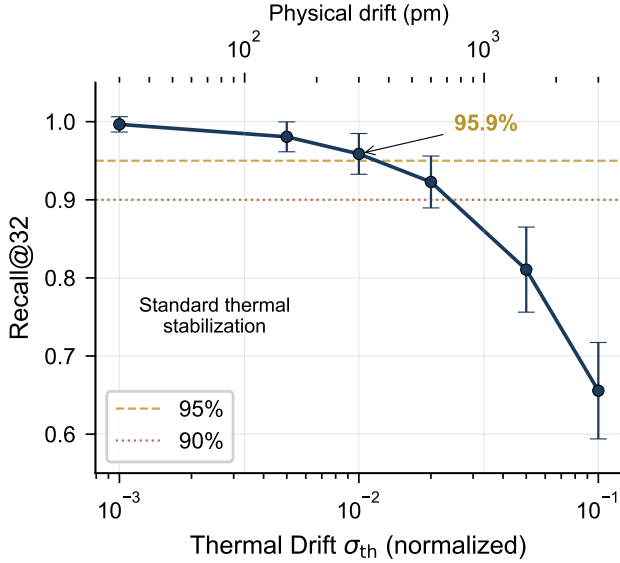


FIG. S2. Recall degradation as a function of thermal drift σ . Recall remains above 95% for $\sigma \leq 0.005$ (corresponding to ~ 150 pm drift), achievable with standard thermal stabilization. At $\sigma = 0.01$ (~ 300 pm), recall is still 94.8%.

TABLE S2. PRISM latency breakdown.

Stage	Latency Notes
DAC	~ 1 ns 4-bit
MZM	~ 0.1 ns Si depl.
Opt. prop.	~ 0.5 ns 5 cm
MRR decay	~ 0.1 ns $Q=10^4$
PD	~ 0.2 ns Ge
TIA+ADC	~ 2 ns 6-bit flash
Top- k	~ 5 ns CMOS
Total	~ 9 ns

TABLE S3. Retrieval head fraction at threshold $\tau = 0.3$ across context lengths. $R_h(\tau)$: percentage of KV heads with $R_h > \tau$. Mean \bar{R}_h : average retrieval ratio across all heads.

Model	Context	$R_h(\tau=0.3)$ (%)	Heads	Mean \bar{R}_h
Qwen2.5-7B	2K	83.9	94/112	0.574
	4K	83.0	93/112	0.560
	8K	91.1	102/112	0.627
	16K	92.9	104/112	0.639
	32K	95.5	107/112	0.656
	65K	92.0	103/112	0.633
Qwen3-8B	128K	98.2	110/112	0.796
	2K	86.5	250/288	0.626
	4K	88.2	254/288	0.652
	8K	89.6	258/288	0.657

Retrieval Head Detailed Results

Crossover Derivation

This section provides the full algebraic derivation of the energy crossover point n^* summarized in Sec. .

The total decode cost per token for a retrieval head consists of two terms:

$$C_{\text{total}} = C_{\text{select}}(n) + C_{\text{fetch}}(n, k), \quad (\text{S8})$$

where C_{select} is the cost of determining which blocks to fetch and C_{fetch} is the cost of reading and computing attention over the selected blocks.

For the **GPU full scan** baseline, no selection is needed ($k = N = n/B$), so the energy cost of reading all n keys is

$$C_{\text{GPU}} = C_{\text{fetch}}^{\text{GPU}}(n, n/B) = 2 d_h n b_{\text{prec}} \cdot E_{\text{byte}}, \quad (\text{S9})$$

where $E_{\text{byte}} \approx 31$ pJ/B is the energy per byte for HBM3 memory access (H100 GPU) [5].

For **Prism**, the cost is

$$C_{\text{PRISM}} = C_{\text{select}}^{\text{PRISM}}(n) + C_{\text{fetch}}^{\text{GPU}}(n, k \cdot B), \quad (\text{S10})$$

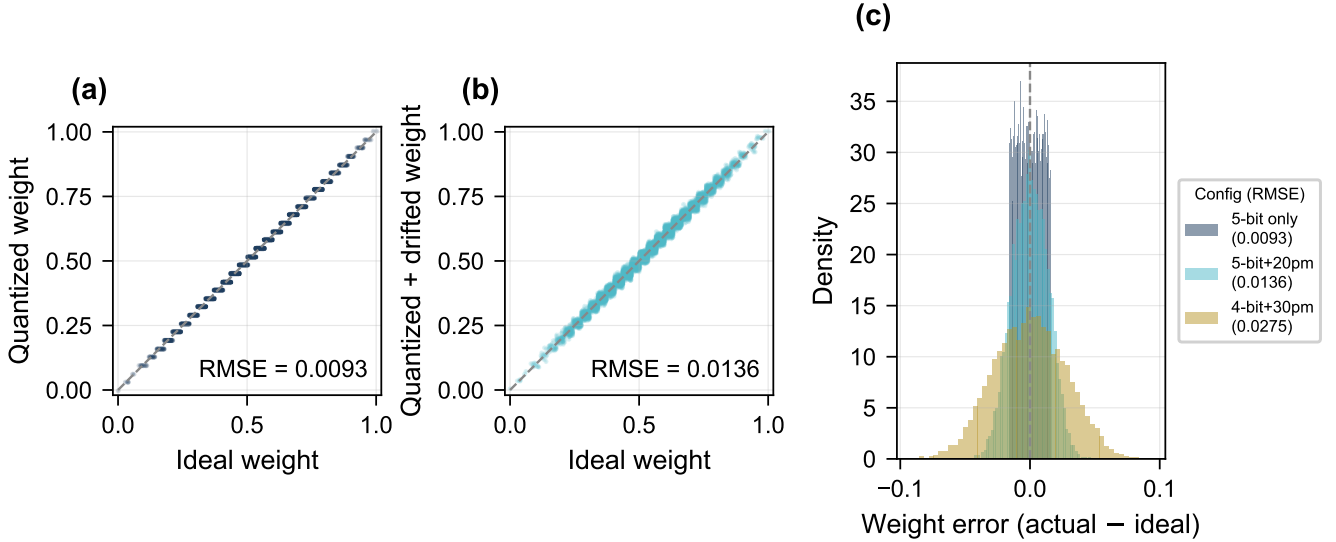


FIG. S3. Weight encoding fidelity under MRR impairments ($d = 32$, $N = 128$). (a) Ideal vs. 5-bit quantised weights in $[0, 1]$: the staircase pattern shows 32 discrete levels with RMSE = 0.009. (b) Adding 20 pm thermal drift and fabrication variation broadens the scatter (RMSE = 0.014). (c) Error histograms for three configurations: 5-bit only, 5-bit with 20 pm drift, and 4-bit with 30 pm drift. Even the pessimistic case concentrates errors within $\pm 5\%$ of the full weight range.

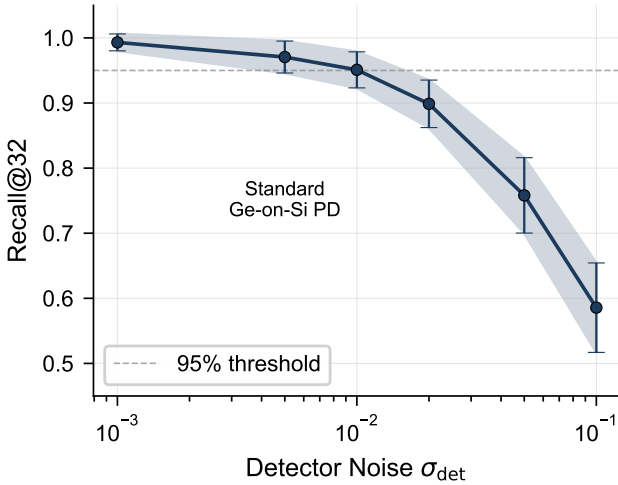


FIG. S4. Recall@8 degradation as a function of photodetector noise σ_{det} ($d = 32$, $N = 500$, 100 trials). Recall remains above the 95% threshold for $\sigma_{\text{det}} \leq 0.01$, achievable with standard Ge-on-Si photodetectors ($\text{NEP} \sim 1 \text{ pW}/\sqrt{\text{Hz}}$).

where $C_{\text{select}}^{\text{PRISM}}$ is the dynamic energy of the photonic evaluation (laser, DAC, modulator, PD, ADC):

$$C_{\text{select}}^{\text{PRISM}} \approx E_{\text{dynamic}}, \quad (\text{S11})$$

Note that on the TFLN platform, the static MRR tuning power is near zero (capacitive EO), so the selection cost is dominated entirely by the dynamic components ($\sim 2290 \text{ pJ}$ per query, table III). The fetch cost is reduced

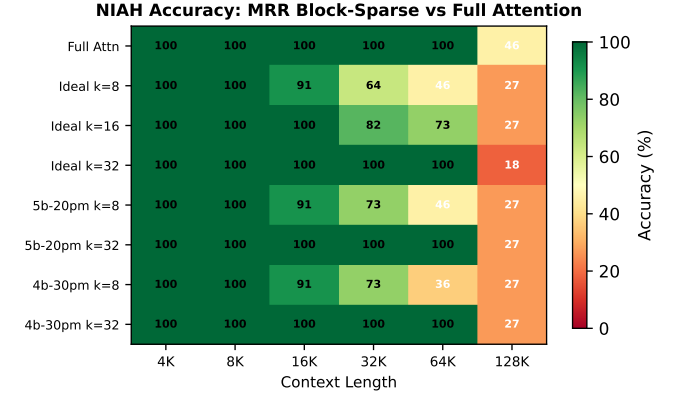


FIG. S5. NIAH accuracy heatmap across context lengths (4K–128K) and MRR configurations. At $k=32$, all MRR variants match full attention perfectly up to 64K. Under the $k=8$ stress test, accuracy degrades gracefully with context length but remains above 90% at 16K. The 128K column shows model-intrinsic degradation (full attention itself drops to 45.5%).

by the selection ratio k/N :

$$C_{\text{fetch}}^{\text{GPU}}(n, k \cdot B) = 2 d_h k B b_{\text{prec}} \cdot E_{\text{byte}}. \quad (\text{S12})$$

The crossover occurs when $C_{\text{PRISM}} < C_{\text{GPU}}$, i.e., when the memory access energy saved by not fetching $(N - k)$ blocks exceeds the energy cost of operating the photonic selector.

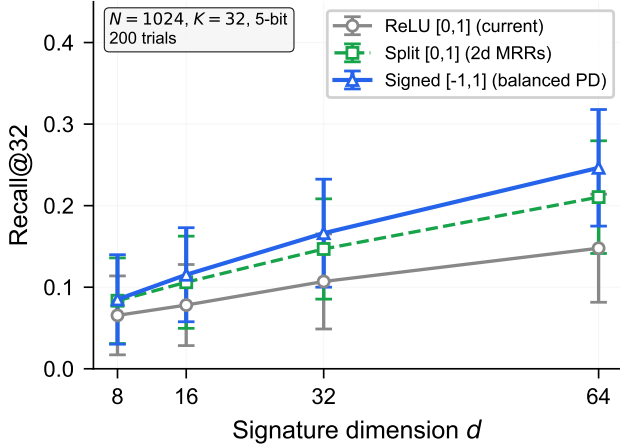


FIG. S6. Signed vs. unsigned recall comparison. Balanced photodetection (signed $[-1, +1]$) consistently outperforms ReLU projection (unsigned $[0, 1]$) and split encoding across all signature dimensions d .

Setting $C_{\text{PRISM}} = C_{\text{GPU}}$ and solving for n yields:

$$n^* = \frac{C_{\text{select}}^{\text{PRISM}}}{2 d_h b_{\text{prec}} E_{\text{byte}} (1 - k B/n^*)}, \quad (\text{S13})$$

which must be solved self-consistently since k and $N = n/B$ both depend on n . In practice, k is a fixed parameter (e.g., $k = 32$), so the selection ratio $k B/n \rightarrow 0$ as $n \rightarrow \infty$, and the crossover simplifies to

$$n^* \approx \frac{C_{\text{select}}^{\text{PRISM}}}{2 d_h b_{\text{prec}} E_{\text{byte}}}. \quad (\text{S14})$$

WDM Channel Limits

The maximum number of WDM channels d is constrained by the MRR free spectral range (FSR), the available optical bandwidth, and inter-channel crosstalk.

Single-FSR constraint. For a TFLN MRR with radius $R = 20 \mu\text{m}$, the FSR is approximately 8.3 nm (at $\lambda_0 = 1550 \text{ nm}$, as in table I). At a channel spacing of $\Delta\lambda_{\text{ch}} = 1.6 \text{ nm}$ (200 GHz on the ITU grid) [6], the maximum number of non-aliased channels within one FSR is

$$d_{\text{max}}^{(1\text{-FSR})} = \left\lfloor \frac{\text{FSR}}{\Delta\lambda_{\text{ch}}} \right\rfloor = \left\lfloor \frac{8.3}{1.6} \right\rfloor = 5. \quad (\text{S15})$$

This is clearly insufficient for the $d = 32\text{--}128$ range targeted by PRISM.

FSR extension techniques. Vernier-coupled dual-ring filters or cascaded MRRs with slightly different radii can extend the effective FSR to $\sim 50 \text{ nm}$ or more [7, 8], limited by the least common multiple of the individual FSRs.

With an extended FSR of 50 nm and $\Delta\lambda_{\text{ch}} = 1.6 \text{ nm}$:

$$d_{\text{max}}^{(\text{Vernier})} = \left\lfloor \frac{50}{1.6} \right\rfloor \approx 30. \quad (\text{S16})$$

Band-limited operation. The usable optical bandwidth depends on the operating band:

- **C-band** (1530–1565 nm): 35 nm \rightarrow practical limit $d \sim 20\text{--}30$ without FSR extension;
- **C+L band** (1530–1625 nm): 95 nm $\rightarrow d \sim 60$.

For $d > 60$, extending to the S-band or using 0.8 nm (100 GHz) channel spacing is necessary, at the cost of tighter crosstalk margins. In practice, achieving $d = 128$ requires both FSR extension and C+L+S band operation, representing a more aggressive photonic design point.

Balanced Photodetection for Signed Weights

The add-drop MRR configuration provides both through-port transmission $T_{\text{through}}(\Delta\lambda)$ and complementary drop-port transmission $T_{\text{drop}}(\Delta\lambda) = 1 - T_{\text{through}}(\Delta\lambda)$ (for a lossless ring). A balanced photodetector pair measures the differential signal:

$$w = T_{\text{through}} - T_{\text{drop}} = 2T_{\text{through}} - 1 \in [-1, +1]. \quad (\text{S17})$$

This mapping naturally encodes signed weights without doubling the MRR count (as required by split encoding) or discarding sign information (as in ReLU projection). The noise model for balanced detection yields shot noise variance $\sigma^2 = 2e\mathcal{R}P_0\Delta f$, independent of the programmed weight, since power is conserved: $P_{\text{through}} + P_{\text{drop}} = P_0$ [1].

Multi-Head Serving with GQA

A natural concern is whether serving all retrieval heads requires replicating the weight bank for each head. In Qwen2.5-7B, 102 out of 112 KV heads are retrieval heads at 8K context (table S3). However, GQA [9] reduces the number of *independent* KV heads to $H_{\text{KV}} = 4$ —each KV head is shared across $H/H_{\text{KV}} = 7$ query heads. The weight bank stores block *signatures* derived from key vectors, so it operates at the KV-head granularity, not the query-head granularity. This means only 4 independent weight bank configurations are needed per layer, not 102. Two strategies can serve these 4 KV heads:

1. **Time-multiplexed reuse.** A single weight bank is reprogrammed sequentially for each of the 4 KV heads. On the TFLN platform, EO tuning settles in $\sim 1 \text{ ns}$ (RC-limited), so reprogramming 4 heads adds only $\sim 4 \text{ ns}$ —negligible compared to the subsequent KV block fetch ($\sim 5 \mu\text{s}$).

2. **Parallel replication.** Four weight banks are deployed in parallel, one per KV head. This requires $4 \times d \times N = 4 \times 64 \times 1024 = 262\,144$ MRs total—a $4\times$ increase over the single-head case but within the scalability limits discussed in [Sec. .](#)

GQA thus reduces the multi-head serving problem from 102 independent banks (one per retrieval head) to just 4, making both time-multiplexed and spatially-parallel approaches practical. For Qwen3-8B ($H_{KV} = 8$), the same argument applies with 8 KV heads, still far below the 258 retrieval heads.

* Corresponding author: yeonsang.park@cnu.ac.kr

[1] B. E. A. Saleh and M. C. Teich, *Fundamentals of Photonics*, 3rd ed. (John Wiley & Sons, 2019).

- [2] S. D. Personick, *Bell System Technical Journal* **52**, 843 (1973).
- [3] H. Jayatileka, K. Murray, M. Caverley, N. A. F. Jaeger, L. Chrostowski, and S. Shekhar, *Journal of Lightwave Technology* **34**, 2886 (2016).
- [4] W. Bogaerts, P. De Heyn, T. Van Vaerenbergh, K. De Vos, S. Kumar Selvaraja, T. Claes, P. Dumon, P. Bienstman, D. Van Thourhout, and R. Baets, *Laser & Photonics Reviews* **6**, 47 (2012).
- [5] J. Choquette, *IEEE Micro* **43**, 9 (2023).
- [6] International Telecommunication Union, Spectral grids for WDM applications: DWDM frequency grid, ITU-T Recommendation G.694.1 (2020).
- [7] A. N. Tait, T. F. de Lima, E. Zhou, A. X. Wu, M. A. Nahmias, B. J. Shastri, and P. R. Prucnal, *Scientific Reports* **7**, 7430 (2017).
- [8] R. Boeck, N. A. F. Jaeger, N. Rouger, and L. Chrostowski, *Optics Express* **18**, 25151 (2010).
- [9] J. Ainslie, J. Lee-Thorp, M. de Jong, Y. Zemlyanskiy, F. Lebron, and S. Sanghai, in *Proceedings of the 2023 Conference on Empirical Methods in Natural Language Processing (EMNLP)* (2023) pp. 4895–4901.